ORIGINAL PAPER

Fractional calculus derivation of a rate-dependent PPR-based cohesive fracture model: theory, implementation, and numerical results

Oliver Giraldo-Londoño · Glaucio H. Paulino · William G. Buttlar

Abstract Rate-dependent fracture has been extensively studied using cohesive zone models (CZMs). Some of them use classical viscoelastic material models based on springs and dashpots. However, such viscoelastic models, characterized by relaxation functions with exponential decay, are inadequate to simulate fracture for a wide range of loading rates. To improve the accuracy of existing models, this work presents a mixed-mode rate-dependent CZM that combines the features of the Park–Paulino–Roesler (PPR) cohesive model and a fractional viscoelastic model. This type of viscoelastic model uses differential operators of non-integer order, leading to power-law-type relaxation functions with algebraic decay. We derive the model in the context of damage mechanics, such that undamaged viscoelastic tractions obtained from a fractional viscoelastic model are scaled using two damage parameters. We obtain these parameters from the PPR cohesive model and enforce them to increase monotonically during the entire loading history, which avoids artificial self-healing. We present three examples, two used for validation purposes and one to elucidate the physical meaning of the fractional differential operators. We show that the model is able to predict rate-dependent fracture process of rubber-like materials for a wide range of loading rates and that it can capture rate-dependent mixed-mode fracture processes accurately. Results from the last example indicate that the order of the fractional differential operators acts as a memory-like parameter that allows for the fracture modeling of long- and short-term memory processes. *The ability of fractional viscoelastic models to model this type of process suggests that relaxation functions with algebraic decay lead to accurate fracture modeling of materials for a wide range of loading rates.*

1 Introduction

The fracture process in many materials is inherently rate-dependent. This rate dependence is due to either bulk-material viscoelasticity, the bond-breakage process in front of the crack tip, or a combination (Bažant and Li 1997). Understanding the underlying mechanisms that produce rate dependence in the fracture process is of importance in several industries, including automotive, aeronautical, and civil, among others.

O. Giraldo-Londoño · G. H. Paulino (✉)
School of Civil and Environmental Engineering, Georgia Institute of Technology, Atlanta, GA, USA
e-mail: paulino@gatech.edu

W. G. Buttlar
School of Civil and Environmental Engineering, University of Missouri, Columbia, MO, USA

For example, the fracturing process of structural adhesives in the automotive industry exhibits rate dependency (Marzi et al. 2009a, b; May et al. 2015), and thus such phenomenon must be accounted for in the design of those adhesives. Likewise, fracture in bituminous materials, such as asphalt concrete, is rate dependent (Kim et al. 2009). Despite extensive previous research in this area, the processes governing rate-dependent fracture are still not fully understood, and thus we recognize the need to perform more studies pertaining to this subject.

Studies conducted in the 1960s and 1970s explored rate-dependence of fracture (Williams 1963, 1965; Knauss 1970; Mueller and Knauss 1971; Maugis and Barquins 1978). Many of those studies, although important for explaining some of the mechanisms that govern rate-dependence of fracture, mainly focused on simple geometries and considered a small fracture process zone (FPZ). Those approaches are not suitable to solve problems involving more complex geometries or loading conditions or problems in which the size of the FPZ is significant. To solve more complex problems, alternative approaches such as cohesive zone models (CZMs) are desirable because they can simulate nonlinear material separation and a large fracture process zone (Park and Paulino 2011). Several rate-independent CZMs have been proposed that assume potential functions based on specific-degree polynomials (Needleman 1987; Freed and Banks-Sills 2008) or exponential-based functions (Needleman 1990a, b; Xu and Needleman 1993). In these models, the shape of the softening portion of the cohesive relationship cannot be easily modified. Several studies, however, have shown that the shape of the softening portion of the CZM significantly affects the simulated fracture behavior (Volokh 2004; Alfano 2006), which indicates that fracture simulations require a model capable of controlling the softening shape of the CZM.

To address the limitations of existing CZMs, this study uses the Park–Paulino–Roesler (PPR) potential-based CZM (Park et al. 2009; Park and Paulino 2012). The PPR model is a potential-based model of general polynomial order able to control the shape of the softening portion of the traction–separation relationships in both the normal and tangential directions. The ability to control the softening shape of the traction–separation relations allows the PPR model to simulate a wide range of failure responses (e.g., quasi-brittle). In addition to have the ability to control the softening shape of the

traction–separation curves, the PPR model can consistently handle different fracture energies and cohesive strengths in modes I and II, which is essential to model mixed-mode fracture (Park et al. 2009).

The original PPR cohesive zone model, as well as many other CZMs, is not able to simulate rate-dependent fracture in its primary form. However, with some additional considerations, rate-independent CZMs can be used to simulate rate-dependent fracture phenomena. For example, a study by Corigliano et al. (2003) investigated the rate-dependent debonding process in composite materials using an exponential-type cohesive model. They enhanced the exponential CZM with a dimensionless interface parameter that was a function of the crack opening velocity. Alternatively, Zhou et al. (2005) used a phenomenological CZM to study dynamic crack propagation of pre-strained PMMA plates. Using a bilinear traction–separation relationship, they constructed a cohesive model in which the final crack opening width (i.e., the crack opening width in which tractions vanish) was a function of the crack tip velocity. They chose this function such that the fracture energy increased exponentially as the crack tip velocity increased while assuming that the cohesive strength remained constant. In contrast, Marzi et al. (2009a) incorporated rate-dependence into their CZM through phenomenological expressions for peak traction and critical energy release rate. They constructed these expressions based upon experimental observations from tapered double cantilever beam tests subjected to various applied loading rates.

Other phenomenological models have been reported in the literature and are of interest in the present investigation. For instance, to address the rate-dependent mixed-mode crack propagation of epoxy adhesives, Makhecha et al. (2009) presented two cohesive models based on perturbations of an exponential function. They constructed the models based on experimental observations of mode I fracture tests performed on compact tension specimens. To simulate the high-speed fracture behavior of a steel alloy, Valoroso et al. (2014) used a cohesive element in which rate dependence was captured through an amplification function of the critical energy release rate. May et al. (2015) developed a mixed-mode rate-dependent cohesive zone model that incorporated their experimental results on both tapered double cantilever beam (TDCB) and tapered end-notched beam bonded with a crash-optimized adhesive. The experiments showed that, as the crack open-

ing rate increased, fracture toughness and cohesive strength in both the normal and tangential directions also increased. Their model represented both the fracture energy and cohesive strengths with phenomenological expressions in terms of the crack opening rate.

The rate-dependent CZMs discussed above are typically derived from a rate-independent CZM by defining their fracture energy, cohesive strength, and/or final crack opening as a function of the crack opening rate. Therefore, those models may neglect some physical processes related to rate-dependent fracture. Other models account for physical processes, such that the FPZ is modeled as a viscoelastic media. For example, some models assume that the FPZ consists of viscoelastic fibrils that become damaged over time (Rahul-Kumar et al. 1999; Allen and Searcy 2001) and others assume that FPZ is represented by nonlinear softening springs and dashpots (Xu et al. 2003a, b). They constructed a mode I rate-dependent CZM by replacing one of the springs of a standard linear solid (SLS) model with a nonlinear softening spring, whose traction–separation behavior followed an exponential function. Although their model was able to fit the obtained experimental results, it predicts infinite fracture energy as the opening rate approaches infinity. Using a similar approach, Musto and Alfano (2013) studied the rate-dependent debonding process in a double cantilever beam (DCB) bonded by an interface of SBR/NR-blend rubber. They developed their model using concepts from both linear viscoelasticity and damage mechanics by first obtaining normal tractions from an SLS model, and then scaling them using a damage-type variable consistent with a rate-independent bilinear CZM in mode I. However, their numerical results were not in good agreement with experimental data obtained from DCB tests performed at various loading rates (Musto and Alfano 2013).

The studies discussed above use classical viscoelastic models that consist of springs and dashpots, and thus they have limited ability to predict the fracture behavior for a wide range of loading rates. Recently, Musto and Alfano (2015) proposed a rate-dependent CZM using fractional viscoelastic theory (Mainardi 2010). Similarly to their previous work (Musto and Alfano 2013), they used an SLS model, but instead of using a dashpot in the Maxwell arm, they used a more general element whose constitutive relationship is defined in terms of differential operators of non-integer order (Mainardi 2010). This generalized element, typically

called *springpot*, can interpolate between a spring and a dashpot. In contrast to their earlier work (Musto and Alfano 2013), results using the fractional viscoelastic model (Musto and Alfano 2015) closely matched the results of experiments performed on DCB test specimens.

It is not surprising that the new cohesive zone model presented by Musto and Alfano (2015) is able to capture the fracture response of an elastomeric material for a wide range of loading rates. That is because rheological models of fractional order, compared to classical viscoelastic models, are able to describe more complex viscoelastic behavior. In particular, fractional viscoelastic models are able to model both short- and long-term hereditary phenomena, which is possible because these models are characterized by relaxation functions of algebraic decay instead of exponential decay[1] (Mainardi 2010), which is consistent with observations made for several materials (e.g., see Kapnistos et al. 2008; Olard and Di Benedetto 2003; Davis et al. 2006, to name a few). As discussed in the subsequent section, viscoelastic models of fractional order have successfully been used to represent the viscoelastic behavior of several materials such as asphalt, polymers, biological tissue, among others. These attributes have motivated us to use a fractional viscoelastic model to represent the rate-dependent response of our mixed-mode cohesive element.

In this study, we combine the features of both the PPR potential fracture model and a fractional viscoelastic model to derive a rate-dependent mixed-mode CZM. We develop the cohesive fracture model in the context of damage mechanics. First, we obtain undamaged normal and tangential tractions from a mixed-mode fractional SLS model and scale them with two scalar damage parameters that we obtain from the mixed-mode PPR cohesive fracture model by Park et al. (2009). Unlike previous studies that only consider mode I fracture (Musto and Alfano 2015), the present model is able simulate the rate-dependent bond-breakage process in front of the crack tip under mixed-mode conditions. Using the present model, we are also able to modify the shape of the softening portion of the traction–separation curves through two shape parameters and to consider different fracture energies and cohesive strengths in modes I and II consistently.

---

[1] Relaxation functions of algebraic decay are ubiquitous in classical viscoelastic models that are based on springs and dashpots.

Another novelty of the present formulation is a method that we introduce to compute the fractional derivatives, which allows for a variable time step. In contrast to traditional methods for numerical computation of fractional derivatives (e.g., see Musto and Alfano 2015; Schmidt and Gaul 2002), our ability to use a variable time step facilitates implementation of our rate-dependent CZM into into a finite element (FE) code that uses variable time stepping algorithms. The results from our model resemble experimentally observed results from both mode I and mixed-mode fracture tests and provide insight regarding meaning and implications of fractional differential operators in rate-dependent fracture analysis. The framework presented in this study can be used to extend existing rate-independent mixed-mode CZMs to capture rate-dependent fracture processes.

The remainder of this paper is organized as follows. First, Sect. 2 provides some theoretical background of fractional calculus and fractional viscoelasticity, and shows that fractional viscoelastic models lead to power-like relaxation functions, typical of long-term hereditary phenomena. Section 3 presents details of the formulation of the mixed-mode rate-dependent CZM. Section 4 presents three comprehensive examples, and Sect. 5 provides some concluding remarks. Three appendices complement the manuscript.

2 Preliminary theoretical considerations

This section describes some of the main concepts related to fractional calculus and their application to fractional viscoelasticity. First, we review the *Riemann–Liouville fractional integral* and use it to obtain the *Caputo fractional derivative*. Then, we discuss the numerical solution of the Caputo fractional derivative, followed by applications of fractional calculus in viscoelasticity. Finally, we use fractional viscoelasticity to generalize the standard linear solid model, typically used in viscoelasticity. For additional details about fractional calculus and/or fractional viscoelasticity, we refer the interested readers to Oldham and Spanier (1974), Miller and Ross (1993), Podlubny (1998), Mainardi (2010).

2.1 Basic concepts of fractional calculus

Consider the Cauchy formula for repeated integration shown below:

$$
\begin{aligned}
{}_0I_t^n f(t) &= \int_0^t \int_0^{\tau_1} \cdots \int_0^{\tau_{n-1}} f(\tau_n)\mathrm{d}\tau_n \cdots \mathrm{d}\tau_1 \\
&= \frac{1}{(n-1)!} \int_0^t (t-\tau)^{n-1} f(\tau)\mathrm{d}\tau.
\end{aligned} \tag{1}
$$

This formula represents the nth repeated integral of the function $f(\tau)$, $\tau \in (0, t)$. For notation purposes, we use the left subscript, 0, and right subscript, t, to indicate that the lower and upper limits of the integral above are $\tau = 0$ and $\tau = t$, respectively, and thus this notation is used in all equations hereafter. We can extend Cauchy's formula from positive integer values of n to any positive real value $\hat{v}$ by substituting $(n-1)!$ with $\Gamma(\hat{v})$ in Eq. (1), in which $\Gamma(\cdot)$ denotes the Gamma function. This substitution leads to the so-called *Riemann–Liouville fractional integral* of order $\hat{v} > 0$,

$$
\begin{aligned}
{}_0I_t^{\hat{v}} f(t) &= \frac{1}{\Gamma(\hat{v})} \int_0^t (t-\tau)^{\hat{v}-1} f(\tau)\mathrm{d}\tau, \\
& \quad t > 0, \ \hat{v} > 0.
\end{aligned} \tag{2}
$$

By construction, when $\hat{v} = n \in \mathbb{N}$, where $\mathbb{N}$ is the set of natural numbers, the Riemann–Liouville fractional integral reduces to the Cauchy formula for repeated integration. This definition of a fractional integral allows us to obtain differential operators of fractional order (Mainardi 2010).

One of these differential operators is the *Caputo fractional derivative* of order $\hat{v} > 0$, which is obtained by applying the Riemann–Liouville integral operator of order $(m - \hat{v})$ to the integer derivative of order m of a function $f(t)$, where $m - 1 < \hat{v} < m$, $m \in \mathbb{N}$, leading to

$$
\begin{aligned}
{}_0D_t^{\hat{v}} f(t) &= {}_0I_t^{m-\hat{v}} \circ D_t^m f(t) \\
&= \begin{cases} \dfrac{1}{\Gamma(m-\hat{v})} \displaystyle\int_0^t \dfrac{f^{(m)}(\tau)}{(t-\tau)^{\hat{v}+1-m}}\mathrm{d}\tau & \text{if } m-1 < \hat{v} < m, \ m \in \mathbb{N} \\ \dfrac{\mathrm{d}^{\hat{v}} f(t)}{\mathrm{d}t^{\hat{v}}} & \text{if } \hat{v} \in \mathbb{N} \end{cases}.
\end{aligned} \tag{3}
$$

The superscript $\hat{v}$ in ${}_0I_t^{\hat{v}} f(t)$ (Eq. 2) and ${}_0D_t^{\hat{v}} f(t)$ (Eq. 3) represents the order of the fractional integral and fractional derivative, respectively. Note that when $\hat{v} \notin \mathbb{N}$, the Caputo fractional differential operator shown in Eq. (3) (as well as other fractional differential operators) becomes non-local because it depends on the behavior of $f(\tau)$ for $\tau \in [0, t]$. In the next subsection, we show different methods used to compute the Caputo fractional derivative and discuss the method adopted in this study.

2.2 Numerical approximation of the Caputo fractional derivative

We present several numerical methods used to evaluate fractional differential operators and fractional differential equations followed by a numerical scheme that we introduce to solve the Caputo fractional derivative. The introduced numerical scheme allows for variable step, which is suitable for implementation in a finite element code using variable time-stepping algorithms. Several algorithms have been proposed to evaluate fractional derivatives and to solve fractional differential equations. Diethelm et al. (2002) introduced a predictor-corrector approach that aims to solve a fractional differential equation of the form $D_t^{\hat{v}} y(t) = f(t, y(t))$. Additional numerical techniques to solve fractional differential equations and to evaluate fractional derivatives is presented by Diethelm et al. (2005). To evaluate the Caputo fractional derivative based on measured data with noise, Murio (2006) presented a regularization technique that leads to a stable evaluation of such derivative. Krishnasamy et al. (2017) presented a methodology to solve fractional differential equations that is based on fractional Taylor basis approximations.

The numerical approaches described above typically use a constant time step to evaluate the fractional derivatives. Here, we present an approach that allows us to use a variable time step to evaluate the Caputo derivative of order $\hat{v} \in (0, 1)$. Consider the following Caputo fractional derivative of order $\hat{v} \in (0, 1)$ of a function $f(t)$ evaluated at $t = t_N$,

$$_0D_t^{\hat{v}} f(t_N) = \frac{1}{\Gamma(1 - \hat{v})} \int_0^{t_N} \frac{\dot{f}(\tau)}{(t_N - \tau)^{\hat{v}}} d\tau, \quad 0 < \hat{v} < 1. \quad (4)$$

To find an approximate expression for this fractional derivative, we first divide the time interval $(0, t_N)$ into N segments, which need not be equally spaced, as shown in Fig. 1.
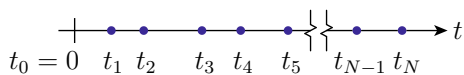

Fig. 1 Time discretization used to evaluate the Caputo fractional derivative in Eq. (4). In contrast to the constant time step required in the Grünwald–Letnikov fractional derivative (Uchaikin 2013), our method employs a variable time step (see "Appendix A")

Next, we approximate $\dot{f}(\tau)$ in each time interval (t_{j-1}, t_j), $j = 1, \ldots, N$, with its backward finite difference approximation, and substitute it into Eq. (4), which leads to the following sum of piecewise integrals:

$$_0D_t^{\hat{v}} f(t_N) \approx \frac{1}{\Gamma(1 - \hat{v})}$$
$$\sum_{j=1}^{N} \frac{f(t_j) - f(t_{j-1})}{t_j - t_{j-1}} \int_{t_{j-1}}^{t_j} (t_N - \tau)^{-\hat{v}} d\tau. \quad (5)$$

After some algebraic maneuvering, Eq. (5) is rewritten as

$$_0D_t^{\hat{v}} f(t_N) \approx \frac{f(t_N) - S_f}{\Gamma(2 - \hat{v}) \Delta t_N^{\hat{v}}}, \quad (6)$$

where

$$S_f = f(t_{N-1}) + \sum_{j=1}^{N-1} \left[f(t_j) - f(t_{j-1}) \right] A_j,$$

$$A_j = \frac{(t_N - t_j)^{1-\hat{v}} - (t_N - t_{j-1})^{1-\hat{v}}}{(t_j - t_{j-1}) \Delta t_N^{-\hat{v}}},$$

$$\Delta t_N = t_N - t_{N-1}. \quad (7)$$

"Appendix A" presents a detailed assessment of the numerical scheme discussed above, which we use to estimate the Caputo fractional derivative of a function $f(t)$.

2.3 Fractional calculus and viscoelasticity

Here, we show the relationship between the Caputo fractional derivative and the behavior of linearly viscoelastic materials with long-term memory, such as polymers. The relaxation behavior of polymers is naturally described by power-law type relaxation functions over a wide range of frequencies (Rubinstein and Obukhov 1993; Kapnistos et al. 2008; Knauss et al. 2008; Milner and Newhall 2010; Uchaikin 2013). In its simplest form, a relaxation function of this type can be defined as

$$G(t) = \frac{a}{\Gamma(1 - \hat{v})} t^{-\hat{v}}, \quad 0 < \hat{v} < 1, \quad t > 0, \quad (8)$$

where $a / \Gamma(1 - \hat{v})$ is a constant measuring the "rigidity" of the material, and $\hat{v}$ is a relaxation parameter. In contrast to relaxation functions based on exponential kernels, a power-law relaxation function undergoes algebraic decay, which we can use to represent materials with long-term memory. From Eq. (8), the

stress–strain relationship for this type of material is given by

$$\sigma(t) = \int_0^t G(t-\tau)\dot{\varepsilon}(\tau)\mathrm{d}\tau = \frac{a}{\Gamma(1-\hat{v})}$$

$$\int_0^t (t-\tau)^{-\hat{v}}\dot{\varepsilon}(\tau)\mathrm{d}\tau, \quad 0 < \hat{v} < 1, \ t > 0, \qquad (9)$$

where $\varepsilon(\tau)$, $\tau \in [0, t]$ is the strain history up to time t. Without loss of generality, we consider only the one-dimensional case (Padovan 1987; Schmidt and Gaul 2002).

Comparing Eqs. (3) and (9), one can observe that the stress, $\sigma(t)$, for a material following a power-law type relaxation function such as that in Eq. (8) can be written in terms of a Caputo fractional derivative with exponent $\hat{v} \in (0, 1)$ (i.e., using $m = 1$ in Eq. (3)) as follows:

$$\sigma(t) = a \, _0D_t^{\hat{v}}\varepsilon(t), \qquad (10)$$

where

$$_0D_t^{\hat{v}}\varepsilon(t) = \frac{1}{\Gamma(1-\hat{v})} \int_0^t \frac{\dot{\varepsilon}(\tau)}{(t-\tau)^{\hat{v}}}\mathrm{d}\tau, \quad 0 < \hat{v} < 1. \qquad (11)$$

Therefore, we can use a stress–strain relationship based on Caputo fractional differential operators to model viscoelastic materials with long-term memory. A constitutive equation of the form shown in Eq. (10) was introduced by Scott-Blair (1947) to describe a viscoelastic material with behavior between that of a Hookean solid and that of a Newtonian fluid. In fact, Eq. (10) represents the behavior of a Hookean solid when $\hat{v} \rightarrow 0$, and a Newtonian fluid when $\hat{v} \rightarrow 1$. The material represented by Eq. (10) gives rise to the more general element known as spring-pot (Mainardi 2010). As depicted in Fig. 2, a spring-pot can be used to represent either a spring or a dashpot, depending on the order of the fractional derivative.

Several studies have shown that a springpot can be represented as an infinite series of springs and dash-pots arranged in a hierarchical manner (Schiessel and Blumen 1993; Schiessel et al. 1994, 1995; Schiessel and Blumen 1995). The hierarchical representation of a springpot explains why, as compared to classical vis-coelastic models, those of fractional order can simulate complex viscoelastic responses using a small amount of parameters. A springpot can be used to generalize
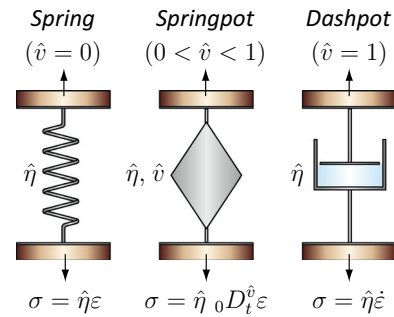

Fig. 2 Stress–strain relationships represented by a springpot. When $\hat{v} \rightarrow 0$, a springpot takes the form of a standard spring, and when $\hat{v} \rightarrow 1$ the springpot takes the form of a standard dashpot

classical viscoelastic models such as Maxwell, Voigt, and Zener (or SLS) models. The generalization can be achieved by substituting the dashpots (found in clas-sical models) with springpots (Mainardi 2010). These types of rheological models have been used to accu-rately simulate the behavior (in frequency domain) of asphalt (Olard and Di Benedetto 2003), acous-tical damping materials (Gourdon et al. 2015), and polymers (Kontou and Katsourinis 2016). In studies by Olard and Di Benedetto (2003), Gourdon et al. (2015), the springpot is referred to as a parabolic creep element. These types of models have also been used to accurately represent the viscoelastic behavior (in time domain) for biological tissue (Davis et al. 2006; Craiem et al. 2008; Dai et al. 2015), polymers (Welch et al. 1999; Kapnistos et al. 2008), among other materials. In this work, we use a fractional gen-eralization of the SLS model because it demonstrates promise as a tool for the realistic simulation of frac-ture in rate-dependent materials (Musto and Alfano 2015).

2.4 Fractional SLS model

A schematic representation of a one-dimensional frac-tional SLS model is illustrated on the top-right corner of Fig. 3. Parameter $\hat{\eta}$ is a viscosity-like quantity and $\hat{v} \in (0, 1)$ defines the order of the Caputo fractional derivative. Both parameters $\hat{\eta}$ and $\hat{v}$ dictate the behav-ior of the springpot. In addition, parameter E defines the stiffness of the equilibrium spring (i.e., the lower spring in the schematic of the fractional SLS model) and parameter c controls the stiffness (cE) of the spring in the fractional Maxwell element (i.e., the upper spring
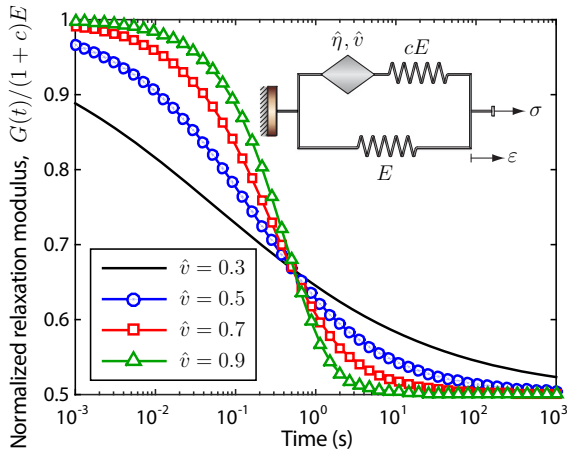
Fig. 3 Relaxation modulus of a fractional SLS model for various orders $\hat{v}$ of the Caputo fractional derivative. For illustration purposes, the relaxation functions shown here are obtained using Eq. (12), with $E = 1$, $c = 1$, and $\hat{\eta} = 1$ (online version in color)

in the schematic of the fractional SLS model). When $\dot{\varepsilon} \to 0$ (slow limit), the stiffness of the fractional SLS model is E, and when $\dot{\varepsilon} \to \infty$ (fast limit), its stiffness is $(1 + c)E$.

The viscoelastic response of the fractional SLS model is characterized by its relaxation modulus, which is given as (Mainardi 2010)

$$G(t) = E\left[1 + cE_{\hat{v}}\left(-(t/\hat{\tau})^{\hat{v}}\right)\right], \tag{12}$$

where:

$$\hat{\tau} = \left[\hat{\eta}/(cE)\right]^{1/\hat{v}} \quad \text{and} \quad E_{\hat{v}}(t) = \sum_{n=0}^{\infty} \frac{t^n}{\Gamma(\hat{v}n + 1)}. \tag{13}$$

Here, $E_{\hat{v}}(t)$ is the Mittag-Leffler function (Mainardi 2010). The behavior of the relaxation modulus given by Eq. (12) is illustrated in Fig. 3 for several values of $\hat{v}$. Note that as $\hat{v}$ increases, we observe more stress relaxation for $t > \hat{\tau}$ (materials with short-term memory), and as $\hat{v}$ decreases, we observe less relaxation for $t > \hat{\tau}$ (materials with long-term memory). Therefore, one can conclude that, with the proper choice of $\hat{v}$, a fractional SLS model can simulate both materials with short- and long-term memory. Materials with the shortest memory correspond to $\hat{v} \to 1$, in which the relaxation function from Eq. (12) reduces to the relaxation function for a classical SLS model[2], i.e., $G(t) = E(1 + ce^{-t/\hat{\tau}})$.

A study by Adolfsson et al. (2005) numerically showed that to obtain the same relaxation function of a fractional SLS model, a classical standard viscoelastic model would need an infinite number of Maxwell elements. This finding is another indication that a rheological model of fractional order, compared to a classical rheological model, can represent complex viscoelastic behavior for a wide range of frequencies (or time) with fewer input parameters, which is one of the reasons for adopting the fractional SLS model in our formulation.

3 PPR-based rate-dependent CZM using fractional calculus

We construct a new mixed-mode rate-dependent CZM in the context of damage mechanics. We begin by obtaining undamaged tractions S_k from a fractional SLS model (Musto and Alfano 2015; Mainardi 2010) and then scale them with two scalar damage-type parameters d_k extracted from the PPR cohesive zone model by (Park et al. 2009). Here, subscript k takes values $k = n$ and $k = t$, which refer to quantities evaluated in the normal and tangential directions to the crack plane, respectively. We use the undamaged tractions, S_k, and the damage parameters, d_k, to obtain the cohesive tractions,

$$T_k = (1 - d_k) S_k, \quad (k = n, t). \tag{14}$$

The model can be visualized as two fractional SLS models, each coupled in series with a damage element, as illustrated in Fig. 4b. In the following subsection, we present details of the derivation of the undamaged tractions, S_k, which are obtained from the normal and tangential fractional SLS models. Next, we elaborate on the derivation of the damage parameters. Finally, we present the final expressions for the proposed mixed-mode rate-dependent cohesive tractions, T_k, and the corresponding material tangent matrix.

3.1 Undamaged tractions S_k

To obtain the undamaged viscoelastic tractions in both normal and tangential directions to the crack plane, we

---

[2] To obtain the standard SLS expression from Eq. (12), we evaluate the Mittag-Leffler function for $\hat{v} = 1$, which reduces to

the Taylor series expansion of the exponential function. That is, $E_{\hat{v}=1}(t) = \sum_{n=0}^{\infty} \frac{t^n}{\Gamma(n+1)} = \sum_{n=0}^{\infty} \frac{t^n}{n!} = e^t$.
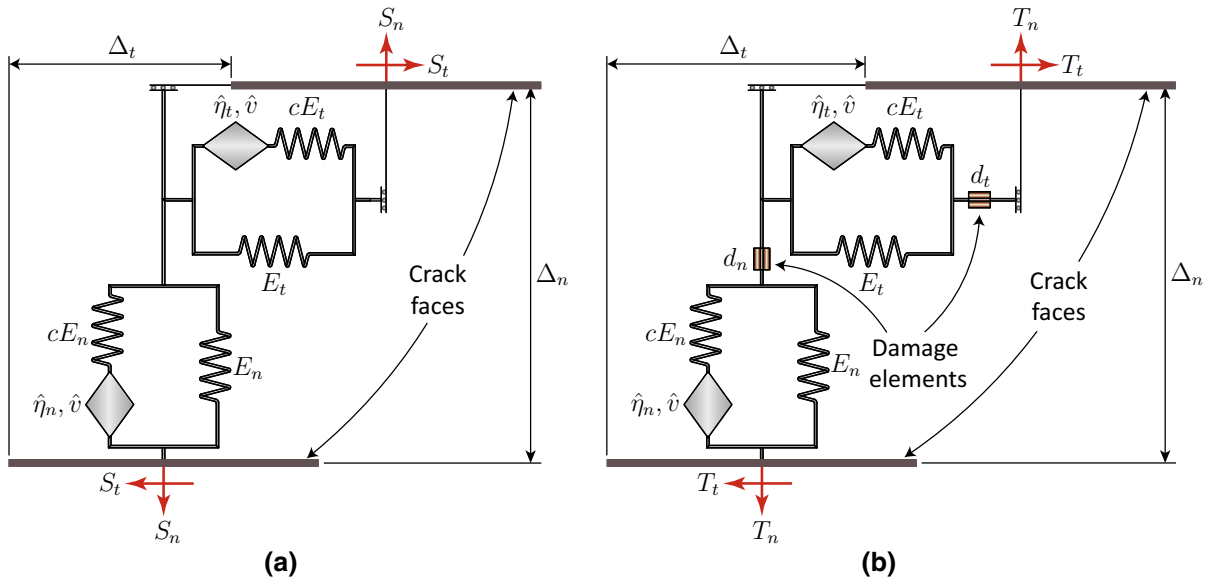
Fig. 4 Rheological representation of the mixed-model rate-dependent CZM: **a** schematic illustration of two fractional SLS models used to obtain the normal and tangential undamaged trac-

tions, S_n and S_t; and **b** schematic illustration of two fractional SLS models, each coupled in series with a damage element, used to obtain the normal and tangential cohesive tractions, T_n and T_t.

use two fractional SLS models as those depicted in Fig. 4a. We assume that in the undamaged stage, normal crack opening displacements produce only normal tractions, and tangential crack opening displacements produce only tangential tractions. In other words, we assume no coupling between normal and tangential tractions in the undamaged stage. To couple normal and tangential cohesive tractions, we employ two damage parameters, as we will discuss in detail in the following subsection.

We obtain the undamaged viscoelastic tractions, S_k, from the solution of the *fractional differential equations*

$$S_k + \hat{\lambda}_k \, {}_0D_t^{\hat{v}}S_k = E_k\Delta_k + \hat{\gamma}_k \, {}_0D_t^{\hat{v}}\Delta_k, \quad (k = n, \ t), \tag{15}$$

where:

$$\hat{\lambda}_k = \hat{\eta}_k/(cE_k), \quad \text{and} \quad \hat{\gamma}_k = \hat{\eta}_k(1+c)/c. \tag{16}$$

To find a solution to Eq. (15), we approximate the fractional derivatives numerically. If the fractional derivatives are approximated using traditional methods, such as the Grünwald–Letnikov approximation (Uchaikin 2013; Musto and Alfano 2015) which uses a constant time step, we expect to encounter a mismatch between the time step used to compute the fractional derivative and that used in the finite element (FE)

model. The mismatch in time steps is more prominent when simulating fracture because the FE model often requires adaptive time-stepping algorithms. Because of the mismatch between time steps, one needs to interpolate between the FE model results at each load step to approximate the fractional derivatives, which introduces additional errors to the numerical solution. For this reason, we approximate the fractional derivatives using a method that allows for variable time step, according to Sect. 2.2.

To solve the fractional differential equation (15), we use the approximate expression for the Caputo fractional derivative given in Eq. (6) to evaluate ${}_0D_t^{\hat{v}}S_k$ and ${}_0D_t^{\hat{v}}\Delta_k$. After some algebraic maneuvering, the expression that we obtain for the undamaged tractions, S_k, are[3]:

$$S_k(t_N) = \hat{E}_k\Delta_k + \Delta S_k^H, \quad (k = n, \ t), \tag{17}$$

where

$$\hat{E}_k = \left(1 + \frac{c\hat{\lambda}_k}{\hat{\lambda}_k + \Gamma(2 - \hat{v})\Delta t_N^{\hat{v}}}\right)E_k,$$

---

[3] We can use an alternative model (e.g., see Giraldo-Londoño et al. 2018) to estimate the rate-dependent undamaged tractions, which requires no computation of fractional derivatives.

$$\Delta S_k^H = \frac{\hat{\lambda}_k S_{S_k} - \hat{\gamma}_k S_{\Delta_k}}{\hat{\lambda}_k + \Gamma(2 - \hat{v})\Delta t_N^{\hat{v}}},$$
(18)

and

$$S_{S_k} = S_k(t_{N-1}) + \sum_{j=1}^{N-1} \left[S_k(t_j) - S_k(t_{j-1}) \right] A_j,$$

$$S_{\Delta_k} = \Delta_k(t_{N-1}) + \sum_{j=1}^{N-1} \left[\Delta_k(t_j) - \Delta_k(t_{j-1}) \right] A_j.$$
(19)

The terms ΔS_k^H in Eq. (17) account for the history of tractions and crack opening displacements between $t = 0$ and $t = t_{N-1}$.

3.2 Normal and tangential damage parameters d_k

As illustrated by Fig. 4b, we adopt two damage parameters, d_k, which we obtain from the PPR cohesive zone model (Park et al. 2009) as conducted in a study by Spring et al. (2016). The damage parameters, d_k, are computed as

$$d_k(\kappa_n, \kappa_t) = 1 - \frac{\hat{T}_k(\kappa_n, \kappa_t)}{E_k \kappa_k}, \quad (k = n, \ t),$$
(20)

where $\hat{T}_k(\kappa_n, \kappa_t)$ are the normal and tangential cohesive tractions from the rate-independent PPR cohesive zone model (Park et al. 2009), which are given by

$$\hat{T}_n(\kappa_n, \kappa_t) = \frac{\Gamma_n}{\delta_n} \left[m \left(1 - \frac{\kappa_n}{\delta_n}\right)^{\alpha} \left(\frac{m}{\alpha} + \frac{\kappa_n}{\delta_n}\right)^{m-1} \right.$$

$$\left. - \alpha \left(1 - \frac{\kappa_n}{\delta_n}\right)^{\alpha-1} \left(\frac{m}{\alpha} + \frac{\kappa_n}{\delta_n}\right)^{m} \right]$$

$$\times \left[\Gamma_t \left(1 - \frac{\kappa_t}{\delta_t}\right)^{\beta} \left(\frac{n}{\beta} + \frac{\kappa_t}{\delta_t}\right)^{n} + \langle \phi_t - \phi_n \rangle \right],$$
(21)

$$\hat{T}_t(\kappa_n, \kappa_t) = \frac{\Gamma_t}{\delta_t} \left[n \left(1 - \frac{\kappa_t}{\delta_t}\right)^{\beta} \left(\frac{n}{\beta} + \frac{\kappa_t}{\delta_t}\right)^{n-1} \right.$$

$$\left. - \beta \left(1 - \frac{\kappa_t}{\delta_t}\right)^{\beta-1} \left(\frac{n}{\beta} + \frac{\kappa_t}{\delta_t}\right)^{n} \right]$$

$$\times \left[\Gamma_n \left(1 - \frac{\kappa_n}{\delta_n}\right)^{\alpha} \left(\frac{m}{\alpha} + \frac{\kappa_n}{\delta_n}\right)^{m} + \langle \phi_n - \phi_t \rangle \right].$$
(22)

As discussed by Spring et al. (2016), the damage parameters in Eq. (20) and the cohesive tractions in Eqs. (21) and (22) are functions of two kinematic quantities, κ_n and κ_t. The first represents the maximum normal crack opening in the loading history, and the second the maximum absolute tangential crack opening in the loading history. These quantities satisfy the following relations (Spring et al. 2016):

$$\kappa_n^{i+1} = \max\left\{\kappa_n^i, \Delta_n^{i+1}\right\} \quad \text{and}$$

$$\kappa_t^{i+1} = \max\left\{\kappa_t^i, \left|\Delta_t^{i+1}\right|\right\},$$
(23)

where in the context of a finite element solution scheme, the superscripts i and $(i + 1)$ refer to the solutions at time increments i and $(i + 1)$, respectively.

We need to satisfy the relations in Eq. (23) to ensure that the damage parameters monotonically increase throughout the loading history (i.e., $d_n^{i+1} \geq d_n^i$ and $d_t^{i+1} \geq d_t^i$), which is consistent with the assumption that no self-healing takes place during fracture. We use Fig. 5 to illustrate the monotonicity condition imposed on the damage parameters. The figure shows typical normal and tangential PPR cohesive tractions $\hat{T}_k(\kappa_n, \kappa_t)$ (Fig. 5a, b) and their corresponding damage parameters $d_k(\kappa_n, \kappa_t)$ (Fig. 5c, d). We observe that the two damage parameters start at zero (when no damage occurs), and monotonically increase to one as the kinematic quantities (κ_n, κ_t) increase. When both the normal and tangential damage parameters approach one, the rate-independent PPR cohesive tractions vanish, indicating complete damage.

The terms E_k in Eq. (20) represent the PPR initial stiffness in the normal and tangential directions, respectively. These expressions were obtained in a study by Spring et al. (2016) and are provided below:

$$E_n = -\frac{\Gamma_n}{\delta_n^2} \left(\frac{m}{\alpha}\right)^{m-1} (m + \alpha) \left[\Gamma_t \left(\frac{n}{\beta}\right)^{n} + \langle \phi_t - \phi_n \rangle\right],$$

$$E_t = -\frac{\Gamma_t}{\delta_t^2} \left(\frac{n}{\beta}\right)^{n-1} (n + \beta) \left[\Gamma_n \left(\frac{m}{\alpha}\right)^{m} + \langle \phi_n - \phi_t \rangle\right].$$
(24)

The parameters α, β, m, n, Γ_n, and Γ_t, used in Eqs. (21)–(21) and in Eq. (24), are the same as in the PPR cohesive model (Park et al. 2009). Parameters α and β, both greater than or equal to one, control the softening shape of the traction–separation relationship in the normal and tangential directions, respectively. The softening portion of the traction–separation relationship is convex if α, $\beta > 2$ or concave if α, $\beta < 2$.

Fig. 5 Typical traction–separation relationships from the PPR cohesive model, and their corresponding normal and tangential damage parameters: **a** normal cohesive traction; **b** tangential cohesive traction; **c** damage parameter in the normal direction; and **d** damage parameter in the tangential direction. For the sake of illustration, the cohesive parameters used here are $\phi_n = 200$ N/m, $\phi_t = 400$ N/m, $\sigma_{\max} = 40$ MPa, $\tau_{\max} = 30$ MPa, $\alpha = 4$, $\beta = 1.5$, $\lambda_n = 0.2$, and $\lambda_t = 0.3$
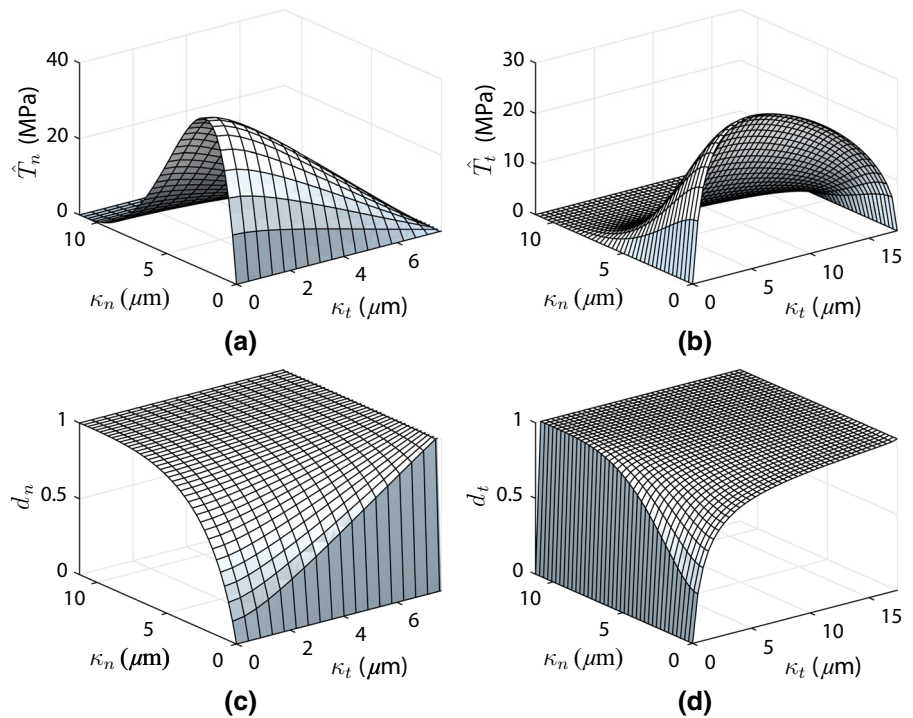
Moreover, the softening behavior is nearly linear if α, $\beta = 2$. Parameters m and n are functions of the shape parameters α and β and two initial slope indicators, λ_n and λ_t, as shown below:

$$m = \frac{\alpha(\alpha-1)\lambda_n^2}{1-\alpha\lambda_n^2}, \quad n = \frac{\beta(\beta-1)\lambda_t^2}{1-\beta\lambda_t^2}. \quad (25)$$

The initial slope indicators correspond to the ratio between the critical crack opening widths and the final crack opening widths:

$$\lambda_n = \delta_{nc}/\delta_n, \quad \lambda_t = \delta_{tc}/\delta_t, \quad (26)$$

where the critical crack opening widths δ_{nc} and δ_{tc} correspond to the crack opening at which the peak tractions are reached in the normal and tangential directions, respectively. The final crack opening widths δ_n and δ_t are obtained as

$$\delta_n = \frac{\phi_n}{\sigma_{\max}}\alpha\lambda_n(1-\lambda_n)^{\alpha-1}\left(\frac{\alpha}{m}+1\right)\left(\frac{\alpha}{m}\lambda_n+1\right)^{m-1},$$
$$\delta_t = \frac{\phi_t}{\tau_{\max}}\beta\lambda_t(1-\lambda_t)^{\beta-1}\left(\frac{\beta}{n}+1\right)\left(\frac{\beta}{n}\lambda_t+1\right)^{n-1}. \quad (27)$$

Energy constants Γ_n and Γ_t are functions of the normal and tangential fracture energies (i.e., ϕ_n and

ϕ_t), respectively. According to Park et al. (2009), the energy constants are

$$\Gamma_n = (-\phi_n)^{\langle\phi_n-\phi_t\rangle/(\phi_n-\phi_t)}\left(\frac{\alpha}{m}\right)^m,$$
$$\Gamma_t = (-\phi_t)^{\langle\phi_t-\phi_n\rangle/(\phi_t-\phi_n)}\left(\frac{\beta}{n}\right)^n, \quad (28)$$

when the normal and tangential fracture energies differ ($\phi_n \neq \phi_t$), and

$$\Gamma_n = -\phi_n\left(\frac{\alpha}{m}\right)^m, \quad \Gamma_t = \left(\frac{\beta}{n}\right)^n, \quad (29)$$

when the normal and tangential fracture energies are the same ($\phi_n = \phi_t$). The bracket $\langle\cdot\rangle$ in Eq. (28) corresponds to the *Macaulay bracket*, $\langle x\rangle = \frac{1}{2}(x+|x|)$.

3.3 Rate-dependent cohesive tractions

We obtain the mixed-mode rate-dependent cohesive tractions of the present study by substituting Eqs. (17) and (20) into Eq. (14), which yields

$$T_k = \frac{\hat{T}_k(\kappa_n,\kappa_t)}{E_k\kappa_k}\left(\hat{E}_k\Delta_k + \Delta S_k^H\right), \quad (k=n,\ t). \quad (30)$$

Fig. 6 Typical behavior of our rate-dependent cohesive model for several prescribed constant crack opening rates: **a** normal cohesive traction and **b** tangential cohesive traction. The representative parameters used here are $\phi_n = 10$ N/m, $\phi_t = 20$ N/m, $\sigma_{\max} = 4$ MPa, $\tau_{\max} = 3$ MPa, $\alpha = 5$, $\beta = 1.5$, $\lambda_n = 0.2$, $\lambda_t = 0.2$, $c = 1$, $\hat{v} = 0.2$, and $\hat{\lambda}_n = \hat{\lambda}_t = 1.3$ s$^{\hat{v}}$ (online version in color)
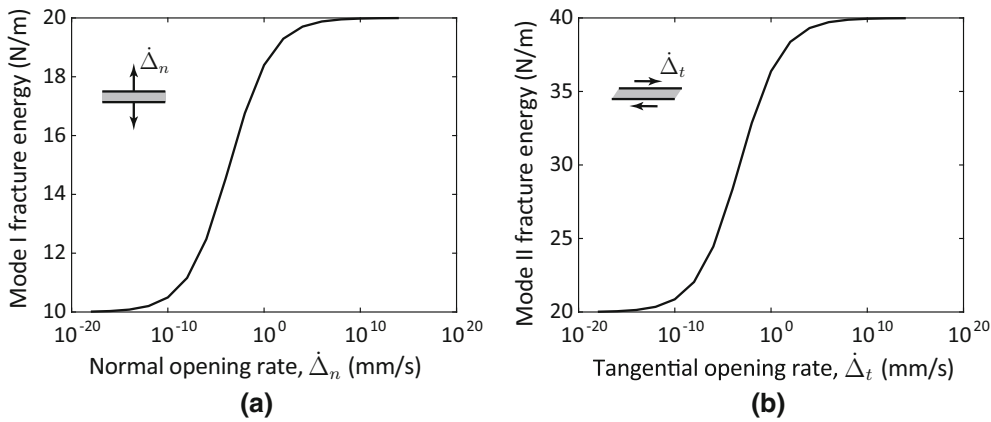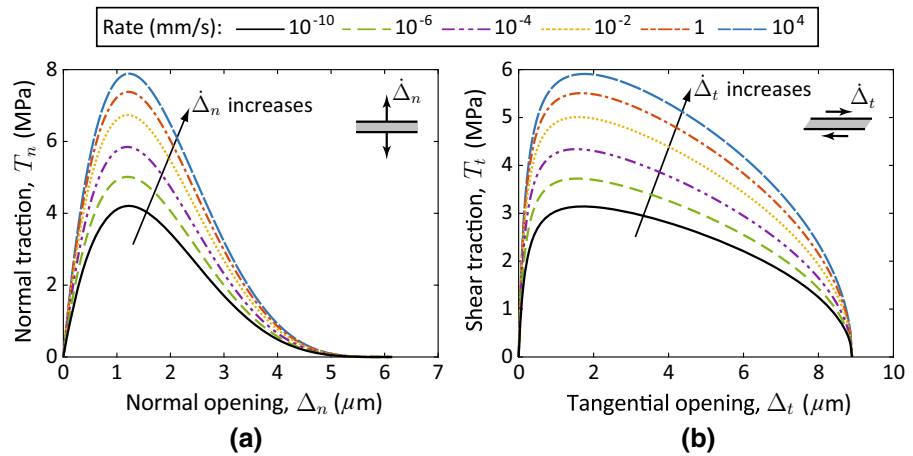

Fig. 7 Fracture energy obtained for several prescribed constant crack opening rates: **a** mode I fracture energy; and **b** mode II fracture energy. The model parameters that we used to obtain these figures are the same as those used to generate Fig. 6

As shown in Fig. 6, we illustrate our rate-dependent cohesive model by plotting the normal and tangential cohesive tractions as functions of the crack opening displacements for several constant crack opening rates in pure modes I and II. The results show that the cohesive tractions increase as the crack opening rate increases. Increase in cohesive tractions as a function of crack opening rate has been observed experimentally in polyurea/steel interfaces (Zhu et al. 2009). In the slow limit case (i.e., when $\dot{\Delta}_k \rightarrow 0$), the maximum normal and tangential cohesive tractions approach $T_n^{\max} = \sigma_{\max} = 4$ MPa and $T_t^{\max} = \tau_{\max} = 3$ MPa, respectively. These peak tractions correspond to the normal and shear cohesive strengths that we adopted for the rate-independent PPR cohesive model (Park et al. 2009), which dictates the behavior of the damage element discussed in the previous subsection. For the fast

limit case (i.e., when $\dot{\Delta}_k \rightarrow \infty$) the normal and tangential cohesive tractions approach $T_n^{\max} = 8$ MPa and $T_t^{\max} = 6$ MPa, respectively, which correspond to $T_n^{\max} = (1+c)\sigma_{\max}$ and $T_t^{\max} = (1+c)\tau_{\max}$, respectively.

We use the results in Fig. 6 to obtain mode I and II fracture energies for several constant prescribed normal and tangential crack opening rates, respectively. Figure 7 shows the computed fracture energies versus the crack opening rates. As one can observe in the figure, both mode I and II fracture energies grow in a sigmoidal shape as the crack opening rates increase. For the slow-limit case, the mode I and II fracture energies approach $\phi_n = 10$ N/m and $\phi_t = 20$ N/m, respectively. These are the fracture energies that we used to define the damage element of the previous subsection. For the fast-limit case, the mode I and II fracture energies

approach $(1 + c)\phi_n$ and $(1 + c)\phi_t$, respectively. Note that, in contrast to previous studies that assume that the fracture energies increase to infinity as the crack opening rates increase, e.g., see Zhou et al. (2005), our model predicts finite fracture energies as the crack opening rates approach infinity. This feature of our model is integral to the representation of real materials. Besides the aforementioned limit behaviors, we observe that both mode I and II fracture energies increase exponentially for a certain range of crack opening rates (linear portions of Fig. 7a, b), which agrees with experimental observations in several studies (e.g., see Zhou et al. 2005; Rahul-Kumar et al. 1999).

The sigmoidal behavior of the mode I and II fracture energies as a function of the loading rate is suitable to model elastomeric materials, but it is inadequate to model the behavior of glassy polymers, which typically become more brittle as the crack opening rate increases (e.g., see Williams 1972; Johnson and Radon 1972; Maugis 1985; Webb and Aifantis 1995; de Gennes 1996). The decrease in fracture energy with increasing crack opening rate may be due to increasing temperatures in the fracture process zone (Williams 1972; Johnson and Radon 1972). An alternative explanation for this phenomenon was recently presented by Alfano and Musto (2017). They indicated that if the total elastic energy is considered as the thermodynamic driving force for damage growth, one may observe that the behavior of the fracture energy can be non-monotonic, which is observed in glassy polymers. Although such consideration could be incorporated, it is out of the scope of the present study, and thus the reader is directed to the aforementioned references.

We test the consistency of our model using the non-proportional loading/unloading crack-opening path shown in Fig. 8. In that path, the CZM is loaded in mode I, then it is unloaded and finally is loaded in mode II until complete failure occurs. The amount of loading in mode I is chosen such that damage in the normal direction is $d_n = 96\%$ (i.e., almost complete failure). The cohesive tractions that we computed based on the given crack-opening path are shown in Fig. 9. From these results, we observe that, as we load and unload in mode I (i.e., region A–B–C from Fig. 8), we obtain an expected traction–separation curve. That is, the normal cohesive traction, T_n, increases until it reaches a peak traction and then decreases (region A–B), which is followed by a linear unloading (region B–C). Once we start loading in mode II (point C), the tangential
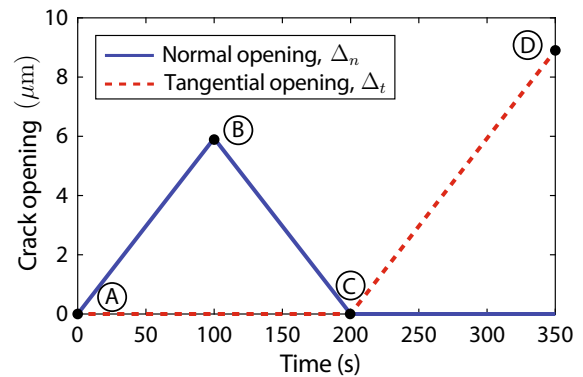

Fig. 8 Non-proportional crack-opening path used to verify the consistency of the rate-dependent cohesive zone model. The loading path consists of mode I loading (A–B), and then by mode I unloading (B–C), followed by mode II loading (C–D)

cohesive tractions, T_t, also behave as expected until complete failure occurs.

The evolution of damage parameters, d_n and d_t, that we obtain from the crack-opening path depicted in Fig. 8 is illustrated in Fig. 10. The figure shows that both normal and tangential damage parameters increase in region A–B (for pure mode I loading), which is expected because both normal and tangential damage parameters are coupled through the kinematic quantities κ_n and κ_t—see Eq. (20). That is, loading in the normal direction affects the behavior of the CZM in the tangential behavior and vice-versa. In addition, both damage parameters remain constant in region B–C (unloading), which is consistent with our assumption that no self-healing is considered in the model. Once mode II loading begins (point C), both normal and tangential damage parameters increase monotonically until complete failure occurs. Because at point C the tangential damage parameter, d_t, is close to one, the tangential cohesive tractions predicted for the model are significantly smaller than the rate independent shear cohesive strength, $\tau_{\max} = 80$ MPa, used to define the damage element. This is an expected response in a physical system in which both normal and tangential damage are coupled.

3.4 Material tangent matrix and related remarks

To implement our model in a finite element software such as ABAQUS (2011), one needs to obtain the material tangent matrix. To obtain such matrix, we differen-

Fig. 9 Cohesive tractions in the **a** normal and **b** tangential directions obtained for the non-proportional crack-opening path of Fig. 8. The CZM parameters used here are $\phi_n = 200$ N/m, $\phi_t = 900$ N/m, $\sigma_{max} = 40$ MPa, $\tau_{max} = 80$ MPa, $\alpha = 3$, $\beta = 1.5$, $\lambda_n = 0.2$, $\lambda_t = 0.3$, $c = 1$, $\hat{v} = 0.2$, and $\hat{\lambda}_n = \hat{\lambda}_t = 1.5$ s$^{\hat{v}}$
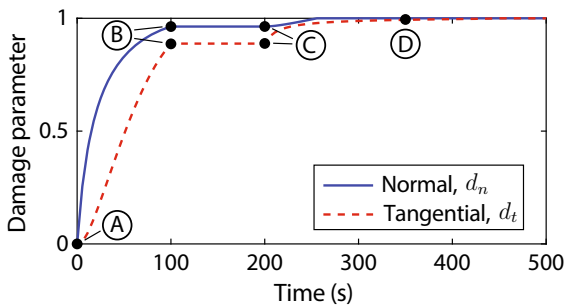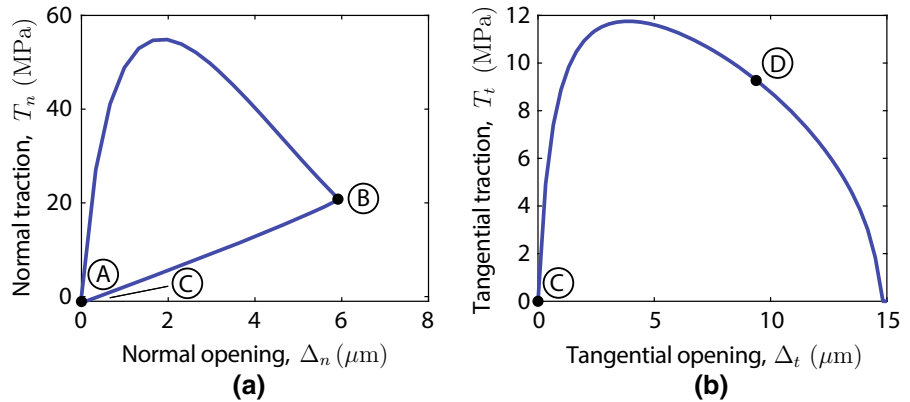

Fig. 10 Evolution of normal and tangential damage parameters, d_n and d_t, obtained for the non-proportional crack-opening path of Fig. 8. The damage parameters are obtained from Eq. (20) using the CZM parameters from Fig. 9

tiate the cohesive tractions, T_k, in Eq. (30), with respect to the crack opening displacements, Δ_k, which leads to

$$\mathbf{D}(\Delta_n, \Delta_t) = \begin{bmatrix} D_{tt} & D_{tn} \\ D_{nt} & D_{nn} \end{bmatrix}, \tag{31}$$

where

$$D_{tt} = \frac{\partial T_t}{\partial \Delta_t} = \frac{S_t}{E_t \kappa_t} \left[\hat{D}_{nn}(\kappa_n, \kappa_t) - \frac{\hat{T}_t(\kappa_n, \kappa_t)}{\kappa_t} \right]$$
$$\frac{\partial \kappa_t}{\partial \Delta_t} + \frac{\hat{E}_t \hat{T}_t(\kappa_n, \kappa_t)}{E_t \kappa_t}, \tag{32}$$

$$D_{tn} = \frac{\partial T_t}{\partial \Delta_n} = \frac{S_t}{E_t \kappa_t} \hat{D}_{tn}(\kappa_n, \kappa_t) \frac{\partial \kappa_n}{\partial \Delta_n}, \tag{33}$$

$$D_{nt} = \frac{\partial T_n}{\partial \Delta_t} = \frac{S_n}{E_n \kappa_n} \hat{D}_{nt}(\kappa_n, \kappa_t) \frac{\partial \kappa_t}{\partial \Delta_t}, \tag{34}$$

$$D_{nn} = \frac{\partial T_n}{\partial \Delta_n} = \frac{S_n}{E_n \kappa_n} \left[\hat{D}_{tt}(\kappa_n, \kappa_t) - \frac{\hat{T}_n(\kappa_n, \kappa_t)}{\kappa_n} \right]$$
$$\frac{\partial \kappa_n}{\partial \Delta_n} + \frac{\hat{E}_n \hat{T}_n(\kappa_n, \kappa_t)}{E_n \kappa_n}. \tag{35}$$

Parameters $\hat{D}_{tt}$, $\hat{D}_{tn}$, $\hat{D}_{nt}$, and $\hat{D}_{nn}$ are the components of the material tangent matrix for the rate-independent PPR cohesive zone model Park and Paulino (2012), and are shown in "Appendix B".

We use the material tangent matrix $\mathbf{D}(\Delta_n, \Delta_t)$ for FE implementation purposes, and so we refer interested readers to Park and Paulino (2012) for a detailed procedure regarding the FE implementation of a two-dimensional linear cohesive element. Note that we included all loading–unloading–reloading scenarios in Eqs. (32)–(35) through the values of $\partial \kappa_n / \partial \Delta_n$ and $\partial \kappa_t / \partial \Delta_t$, which we obtain from Eq. (23) as follows:

$$\frac{\partial \kappa_n}{\partial \Delta_n} = \begin{cases} 1 & \text{if } \Delta_n = \kappa_n, \\ 0 & \text{if } \Delta_n < \kappa_n \end{cases},$$
$$\frac{\partial \kappa_t}{\partial \Delta_t} = \begin{cases} \Delta_t / |\Delta_t| & \text{if } |\Delta_t| = \kappa_t \\ 0 & \text{if } |\Delta_t| < \kappa_t \end{cases}. \tag{36}$$

Equations (36) show that the kinematic quantities κ_n and κ_t only vary under pure loading conditions, but they remain constant if unloading/reloading occurs. The values of $\partial \kappa_n / \partial \Delta_n$ and $\partial \kappa_t / \partial \Delta_t$ (which dictate the evolution of κ_n and κ_t) are illustrated in Fig. 11.

4 Examples and discussion

Here, we present and discuss three examples to test our mixed-mode rate-dependent CZM. In the first example, we validate our model by comparing numerical results with those from rate-dependent DCB tests conducted by Musto and Alfano (2015). In the second example, we conduct a rate-dependent mixed-mode test on a compact tension/shear (CTS) specimen and compare our numerical results with experimental results obtained
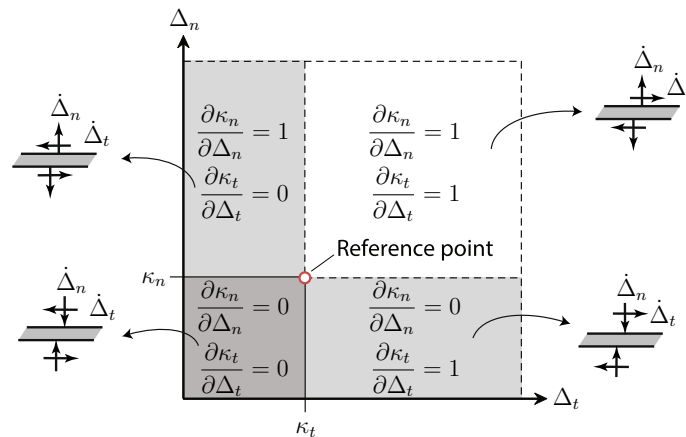
Fig. 11 Given the maximum normal and tangential crack opening during the loading history (reference point), four possible loading scenarios may occur. For *pure loading* (*white region*), both $\partial\kappa_n/\partial\Delta_n = 1$ and $\partial\kappa_t/\partial\Delta_t = 1$; for *partial unloading* (*light gray regions*), $\partial\kappa_n/\partial\Delta_n = 1$ and $\partial\kappa_t/\partial\Delta_t = 0$ when $\Delta_n > \kappa_n$ and $\Delta_t < \kappa_t$, and $\partial\kappa_n/\partial\Delta_n = 0$ and $\partial\kappa_t/\partial\Delta_t = 1$ when $\Delta_n < \kappa_n$ and $\Delta_t > \kappa_t$; and for *pure unloading* (*dark gray region*), both $\partial\kappa_n/\partial\Delta_n = 0$ and $\partial\kappa_t/\partial\Delta_t = 0$. This illustration shows only positive values of Δ_t; therefore, to account for both positive and negative values of Δ_t, the values of $\partial\kappa_t/\partial\Delta_t$ shown here need to be multiplied by sign(Δ_t)—adapted from Spring et al. (2016)

by Liechti and Wu (2001). In the third example, we perform a parametric analysis to investigate the effect of the model parameters in the behavior of a fiber reinforced composite. We use the third example to elucidate the meaning of the order of the Caputo fractional derivative and its relevance in rate-dependent fracture simulations[4].

4.1 Double cantilever beam test

In this example, we compare the numerical results from our model to those from DCB tests performed at various loading rates. We obtain the experimental results from a study by Musto and Alfano (2015), who performed several DCB tests with geometry and load application points, as depicted in Fig. 12a. The geometry of the DCB tests consists of two steel arms partially bonded with a styrene butadiene rubber interface. Each steel arm is 8 mm thick, 25 mm wide, and 200 mm long, and the rubber interface is 1 mm thick, 120 mm long. Musto and Alfano (2015) performed DCB debonding tests at several prescribed constant cross-head displace-

ment rates ranging from 0.01, 0.1, 1, 10, 100, to 500 mm/min.

To compare our results to those of the experimental data from Musto and Alfano (2015), we created six FE models, each of which corresponds to one of the prescribed cross-head displacement rates. The mesh and boundary conditions for each FE model are illustrated in Fig. 12b. We impose a constant velocity boundary condition at the load application points. The magnitude of the velocity imposed at these points corresponds to each of the prescribed cross-head displacement rates in the DCB tests.

In addition to mesh and boundary conditions, we define material properties in our FE models. We model the steel arms using a linear elastic material with Young's modulus of 200 GPa and Poisson's ratio of 0.3. In addition, we model the rubber interface using our mixed-mode rate-dependent CZM and select an appropriate set of model parameters to match the experimental results by Musto and Alfano (2015). Table 1 shows the set of input parameters for the rate-dependent elements used in our FE models. Because the DCB tests are dominated by mode I fracture, we arbitrarily choose the same model properties in the normal and tangential directions. Ideally, those arbitrary parameters should be obtained from proper fracture testing (Reeder and Crews 1990).

---

[4] To obtain the results shown in all the examples, we implemented our rate-dependent CZM as a user-defined element (UEL) subroutine in the commercial FE software ABAQUS (2011).

Fig. 12 Description of the double cantilever beam (DCB) model: **a** geometry and load application points (all dimensions are in mm) and **b** finite element mesh and boundary conditions. We discretize the steel arms using 800 four-node quadrilateral plane strain elements and the rubber interface using 60 zero-thickness rate-dependent cohesive elements
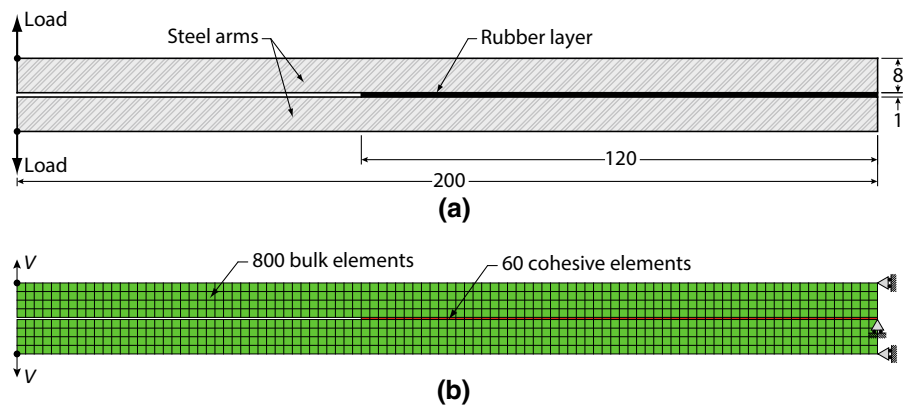

Table 1 Fracture parameters for the cohesive elements used to model the rubber interface in the DCB test

Mode I fracture energy, ϕ_n (N/mm)	2.8
Mode II fracture energy, ϕ_t (N/mm)	2.8
Normal cohesive strength, σ_{max} (MPa)	1.2
Tangential cohesive strength, τ_{max} (MPa)	1.2
Non-dimensional shape parameters, $\alpha = \beta$	3.5
Initial slope indicators, $\lambda_n = \lambda_t$	0.45
Order of the fractional derivative, $\hat{v}$	0.3
Stiffness parameter, c	8.5
Normal and tangential springpot viscosity parameter, $\hat{\lambda} = \hat{\eta}_k/(cE_k)$	3.5

Figure 13 shows both numerical and experimental results for the DCB tests at various loading rates. The results show that the peak load increases as the applied cross-head displacement rate increases. However, for the chosen set of fracture parameters, our model slightly underestimates the experimental peak load for lower rates (e.g., less than 10 mm/min) and slightly overestimates the experimental peak load for higher rates (e.g., more than 10 mm/min). Although we could improve our model predictions by further calibrating the set of fracture parameters (Shen and Paulino 2011a, b), this is beyond the scope of the present study.

Figure 14 presents a typical result from one of the FE simulations, which we use to illustrate the delamination process in one of the DCB tests. This figure shows the evolution of the von Mises stress and the deformation history of one of the DCB tests corresponding to an applied rate of 1 mm/min. Here, we observe that the von Mises stress increases between points A and C,

decays smoothly between points C and E, and drops drastically after point E. The drop in stresses is consistent with the drop in the applied load, which results from the loss of the ligament length bonding the two steel arms.

4.2 Mixed-mode rate-dependent rubber/metal debonding

In this example, we simulate the quasi-static mixed-mode debonding process between rubber and metal. The numerical results obtained from our mixed-mode rate-dependent CZM are compared against the experimental results obtained by Liechti and Wu (2001). Based on their study, we use the compact tension/shear (CTS) specimen to simulate the rate-dependent fracture test. The CTS specimen geometry (Wu 1999) and the finite element discretization are shown in Fig. 15.

The loading is applied as indicated by Liechti and Wu (2001), such that we first apply a normal displacement, u_y, in a stepwise manner, followed by a tangential displacement, u_x, which is applied at a constant rate. We consider both positive and negative shear displacements in this study, and in both cases, we first apply a normal displacement ($u_y = 1.5$ mm) linearly over a time period of 0.05 s followed by a shear displacement with a rate of $\dot{u}_x = 0.01$ mm/s for the positive shear test or $\dot{u}_x = -0.02$ mm/s for the negative shear test. The rates of shear displacement used here are consistent with the shear rates of $\dot{\gamma} = 5 \times 10^{-3}/s$ and $\dot{\gamma} = 1 \times 10^{-2}/s$ reported by Liechti and Wu (2001) for the positive and negative shear experiments, respectively. We wait 100 s between application of the nor-

Fig. 13 Load versus
cross-head displacement
curves for the double
cantilever beam test at
several applied opening
rates. Experimental results
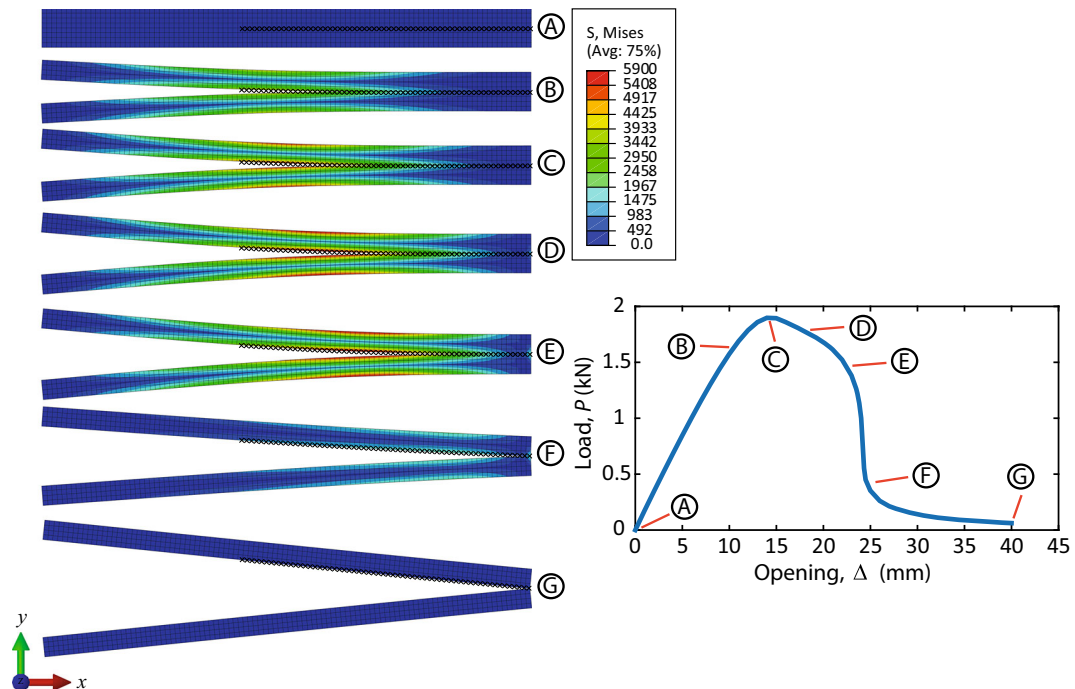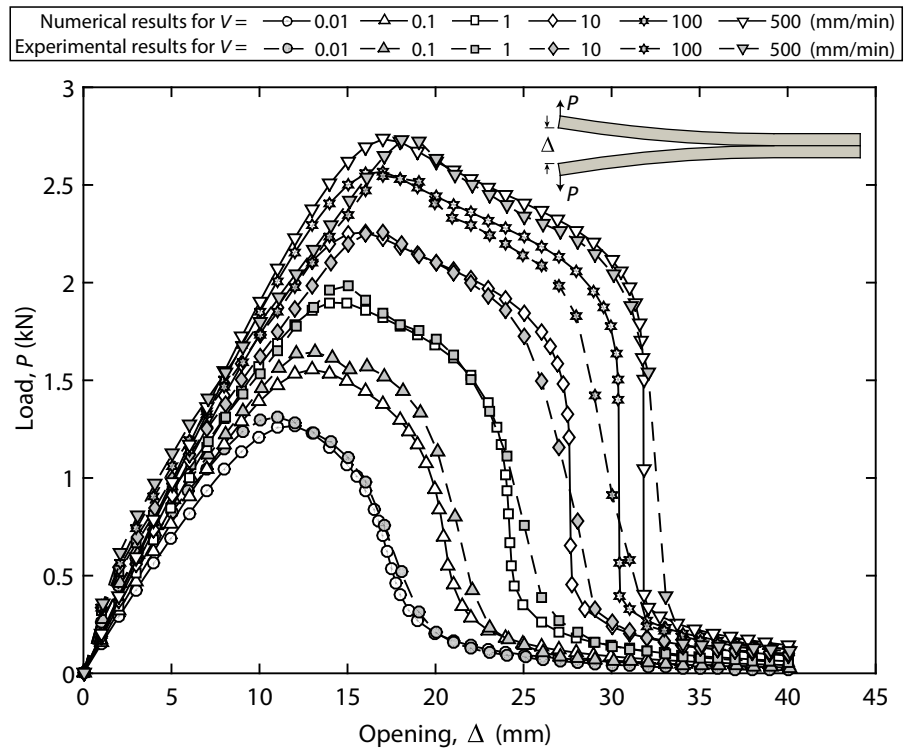are obtained from Musto
and Alfano (2015)

Fig. 14 Evolution of von Mises stresses (kPa) on a typical DCB test (left) for various points during the loading history (right) (online version in color)
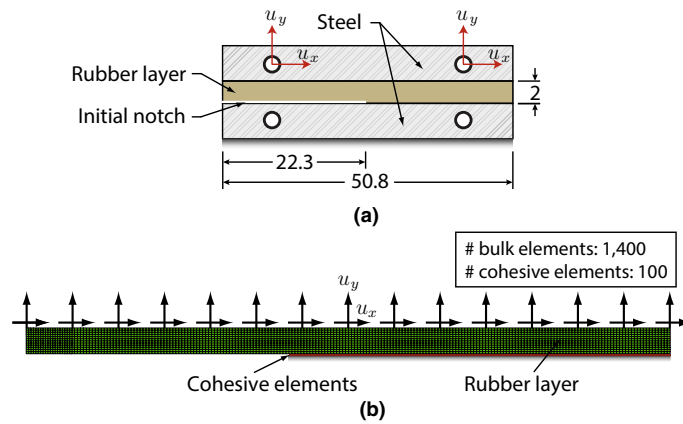
Fig. 15 Geometry of the CTS specimen and finite element discretization used to study the mixed-mode rate-dependent debonding process between rubber and steel: **a** a 2D representation of the CTS geometry (dimensions is mm), and **b** the finite element mesh and boundary conditions used in the simulation. The rubber layer is discretized using 1400 four-node plane stress elements and the debonding layer using 100 zero-thickness rate-dependent (or rate-independent) cohesive elements

mal and the shear displacements, which helps to dissipate some of the viscoelastic stresses in the bulk material induced by the fast application of the normal displacement. This strategy avoids large jumps in both the normal and shear loads that occur in the numerical model when the normal displacement is applied too fast.

The behavior of the rubber (bulk material) is simulated using a visco-hyperelastic material model that uses a three-term incompressible Ogden model (Ogden 1972) with stored-energy density function of the form[5]

$$W = \sum_{i=1}^{3} \frac{2\mu_i}{\alpha_i^2}(\lambda_1^{\alpha_i} + \lambda_2^{\alpha_i} + \lambda_2^{\alpha_i} - 3), \tag{37}$$

where λ_i, $i = 1, 2, 3$ are the principal stretches, and μ_i and α_i are material parameters. We use the parameters shown in Table 2 to define the hyperelastic behavior of rubber[6]. The viscoelastic response of rubber is represented by a 14-term Prony series, whose terms are given in Liechti and Wu (2001).

We simulate the behavior of the rubber/steel interface using the mixed-mode rate-dependent cohesive element derived in Sect. 3. The material parameters

Table 2 Parameters used to describe the hyperelastic behavior of rubber

Term	μ_i (MPa)	α_i
1	0.103	0.5
2	2.45×10^{-4}	8.91
3	0.447	-2

Table 3 Fracture parameters used to simulate the mixed-mode rate-dependent rubber/metal debonding problem

Mode I fracture energy, ϕ_n (N/mm)	0.87
Mode II fracture energy, ϕ_t (N/mm)	3.05
Normal cohesive strength, $\sigma_{\max}$ (MPa)	2.0
Tangential cohesive strength, $\tau_{\max}$ (MPa)	2.4
Non-dimensional normal shape parameter, α	3.0
Non-dimensional tangential shape parameter, β	3.5
Initial slope indicators, $\lambda_n = \lambda_t$	0.05
Order of the fractional derivative, $\hat{v}$	0.3
Stiffness parameter, c	1.49
Normal and tangential springpot viscosity parameter, $\hat{\lambda} = \hat{\eta}_k/(cE_k)$	1.8

that we use to represent the rate-dependent debonding process are given in Table 3. These parameters are obtained by trial and error, such that we are able to approximate the experimental results. We also simulate the debonding behavior of the rubber layer using the rate-independent PPR model (Park et al. 2009; Park and Paulino 2012). To obtain the results from the rate-

---

[5] The form of the stored energy function (37) is that used in ABAQUS (2011) and differs from the form the one used by Liechti and Wu (2001).

[6] Note that the numerical values in Table 2 differ from those reported by Liechti and Wu (2001) because the form of the Ogden stored energy function used in their work differs from that given in Eq. (37).

independent CZM, we scale the mode I and II fracture energies and cohesive strengths from Table 3 to account for the expected increase of fracture energy and cohesive strength due to the applied loading rates. The parameters used for the rate-independent PPR model are $\phi_n = 2.02$ N/mm, $\phi_t = 7.08$ N/mm, $\sigma_{\max} = 4.64$ MPa, $\tau_{\max} = 5.57$ MPa, $\alpha = 3.0$, $\beta = 3.5$, and $\lambda_n = \lambda_t = 0.05$.

Figure 16 shows both the numerical and experimental crack opening displacement (COD) profiles for the positive and negative shear experiments, at the onset of crack initiation and for an instant during crack growth. Due to the finite rotations allowed in the simulations, the numerical results are able to capture the "Z"-shaped crack opening profile obtained experimentally for the positive shear case. The numerical COD profiles obtained with the rate-dependent CZM agree well with those obtained experimentally both for crack initiation and during crack growth and for both the positive and the negative shear experiments. However, the results

from the rate-independent PPR model only agree well with the experimental results for the negative shear experiment. Because the PPR model has no viscoelastic behavior built in, it cannot simultaneously predict the behavior from both positive and negative shear experiments using a single set of fracture parameters.

As depicted in Fig. 17, we also obtain crack separation profiles in both normal and shear directions, during crack initiation and crack growth. For the positive shear experiments (Fig. 17a, b), $\Delta_x < \Delta_y$ during crack initiation and $\Delta_x > \Delta_y$ during crack growth. That is because during crack growth, the crack profile acquires a "Z" shape, which allows for larger displacements in the horizontal direction than in the vertical direction. The results from the negative shear experiment (Fig. 17c, d) show that $|\Delta_x| > \Delta_y$ both during crack initiation and during crack growth. That is because the negative shear experiment requires more energy than the positive shear experiment to debond the rubber layer from the steel substrate, and thus, at the onset of debonding,

Fig. 16 Numerical and experimental crack-opening displacements for the positive shear (top) and negative shear (bottom) tests during: **a** and **c** crack initiation, and **b** and **d** crack growth. The results for the rate-independent CZM are found using the PPR CZM (Park et al. 2009). The location $x = 0$ mm corresponds to the notch tip
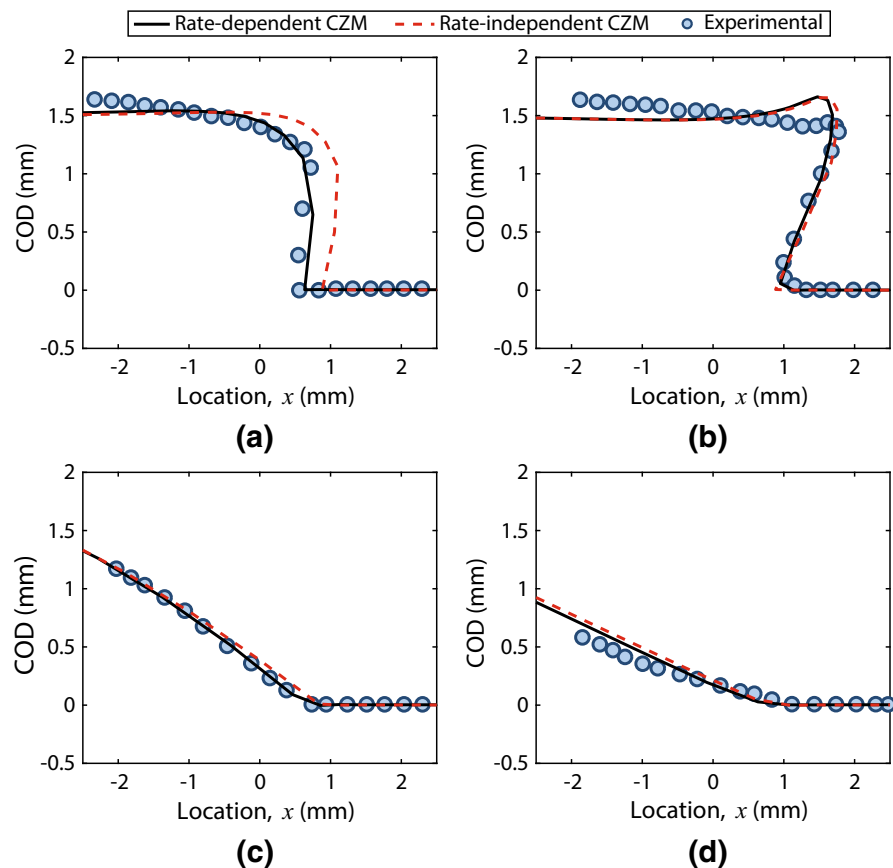
Fig. 17 Crack separation profiles for modes I and II obtained from the simulated mixed-mode fracture tests with positive shear (top) and negative shear (bottom) during: **a** and **c** crack initiation, and **b** and **d** crack growth. The numerical results for the rate-independent CZM are obtained using the PPR CZM (Park et al. 2009). In the results displayed here, the location $x = 0$ mm corresponds to the notch tip
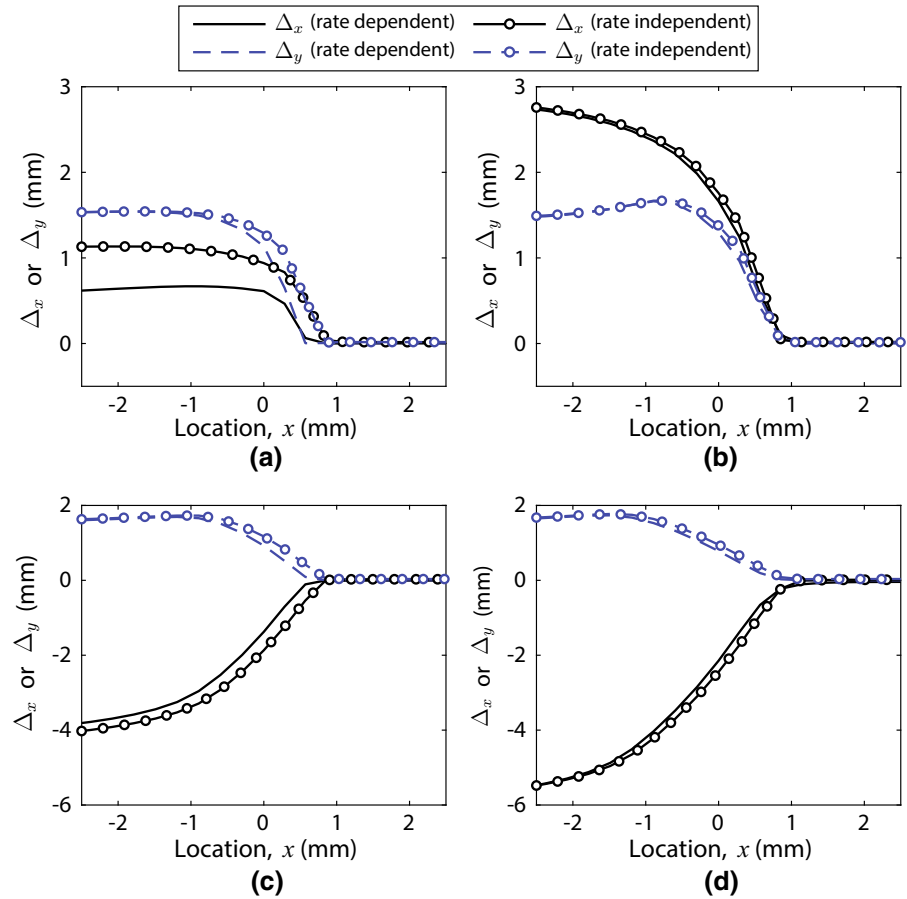
the rubber layer is already considerably stretched in the horizontal direction for the negative shear experiment. As expected from the results shown in Fig. 16, the normal and tangential crack opening displacements from the rate-independent CZM are larger in magnitude than those from the rate-dependent CZM.

In addition to COD and crack-opening profiles, we also compute the time histories of applied loads in both shear and normal directions, as shown in Fig. 18. The predicted shear load behaves almost linearly for both the positive and the negative shear experiments (e.g., see Fig. 18a and c), which agrees with observations by Liechti and Wu (2001). The linear response is attributed to the behavior of the bulk material obtained from the Ogden model. As indicated in Fig. 18b, the change in normal load, which is obtained by subtracting the normal preload due to u_y from the current normal load, agrees well with the experimental measurements for the positive shear experiment, but over-predicts the exper-

imental measurements for the negative shear experiment. Over-prediction in the negative shear experiment, in which large shear strains are required to cause debonding, is expected based on the findings of Liechti and Wu (2001). In Fig. 7e of their paper, they show that the numerical model for the bulk over-predicts normal stresses when large shear strains are applied.

4.3 Rate-dependent matrix/fiber debonding

The following example investigates the rate-dependent debonding behavior of a matrix/fiber interface. We perform an analysis on a unit cell in the form of a regular hexahedron with a cylindrical inclusion, shown in Fig. 19a. We analyze a unit cell under equi-biaxial tension and assume plane strain conditions. Because of symmetry, we model a quarter of the domain (Fig. 19b). The FE mesh and boundary conditions that we use for
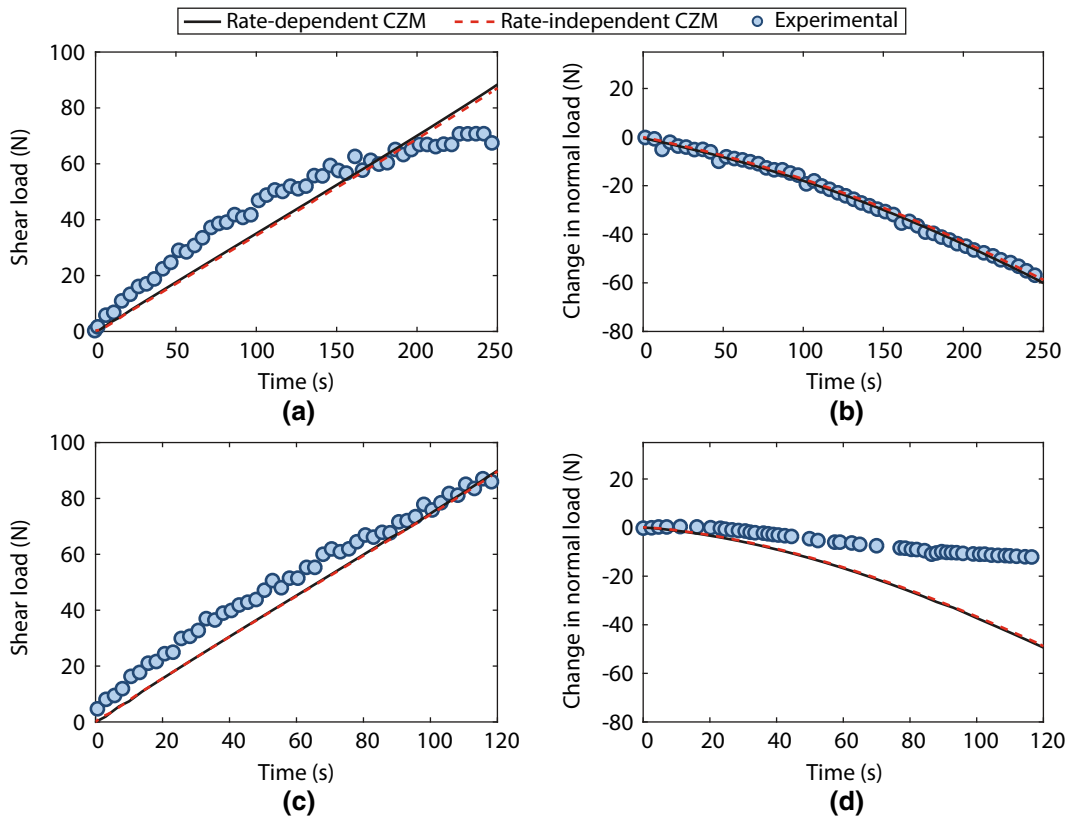
Fig. 18 Numerical and experimental load histories for the mixed-mode fracture tests with positive shear (top) and negative shear (bottom): **a** and **c** shear load, and **b** and **d** change in normal load. The numerical results for the rate-independent CZM are obtained using the PPR CZM (Park et al. 2009)
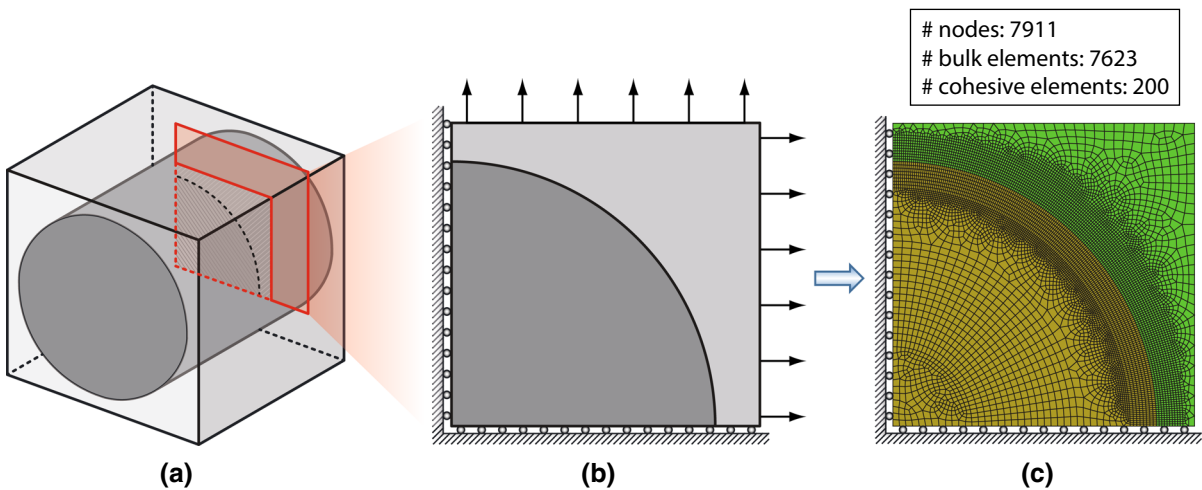

Fig. 19 Description of the model used to study the rate-dependent matrix/fiber debonding process: **a** A 3D representation of the unit cell, **b** a slice containing one quarter of the cross sec-tion used to model the geometry, and **c** the finite element mesh and boundary conditions used in the simulations

this problem are shown in Fig. 19c. Ngo et al. (2010) and Park and Paulino (2012) studied this problem, but they neglected the effects of the loading rate. The study by Ngo et al. (2010) analyzed multiple fiber radii and that by Park and Paulino (2012) focused on a fiber radius of $a_p = 2$ cm. In this example, we use the same fiber radius as that used by Park and Paulino (2012) and assume that the volume fraction of the fiber equals 0.6.

Similarly to Park and Paulino (2012), our study assumes that the elastic modulus of the fiber is $E_p = 40$ GPa and the elastic modulus of the matrix is $E_m = 20$ GPa. We also assume that both the fiber and the matrix have a Poisson's ratio $v_p = v_m = 0.25$. The elastic properties that we selected for the matrix and the fiber are representative of a Polyvinyl Alcohol-Engineered Cementitious Composite (PVA-ECC) (Tosun-Felekoğlu et al. 2014; Kang and Bolander 2016). However, the purpose of the current example is not to study a given particular composite, but instead is to elucidate the effects of cohesive zone model parameters, particularly those from the fractional SLS model.

Because the problem studied herein is dominated by mode I fracture, we arbitrarily assume the same fracture properties in modes I and II to define the properties of the rate-dependent cohesive elements. In the present analysis, we fix the material properties that determine the behavior of the damage elements and vary those that determine the behavior of the fractional SLS model. We vary the properties of the fractional SLS model in order to analyze their effects on the rate-dependent debonding process at the matrix/fiber interface. To determine the behavior of the damage elements, we assume $\phi_n = \phi_t = 100$ N/m, $\alpha = \beta = 3$, $\lambda_n = \lambda_t = 0.1$, and $\sigma_{max} = \tau_{max} = 10$ MPa.

To examine the effects of the loading rate, we move the free faces of the unit cell at several constant speeds in the directions indicated by the arrows in Fig. 19b. The FE model results allow us to obtain the average macroscopic stress–strain curves for each applied velocity and considering the range of the fractional SLS model parameters (i.e., for the values of $\hat{\lambda}_k$, c, and $\hat{v}$). We compute the average macroscopic strains as $\bar{\varepsilon} = Vt/L_0$, where V is the applied velocity at the free faces of the unit cell, t is time, and L_0 is the initial (undeformed) length of the unit cell. Furthermore, we obtain the macroscopic stresses by averaging the reaction forces at the nodes to which the velocity boundary

condition is applied and then normalizing with respect to the undeformed area of the free faces.

Figure 20 presents the FE results for the case of $\hat{v} = 0.3$. From these results, we observe that the initial slopes of the stress–strain curves are independent of the applied velocity, which indicates that for lower strain levels, the elastic behavior of both the matrix and the particle control the macroscopic stress strain response of the composite. This linear portion extends as the applied velocity increases, but as the strain increases, the stress–strain curves deviate from their initially linear behavior until the peak stress is reached. After the peak stress is reached, the macroscopic stress decreases (stress softening), but for higher applied velocities (e.g., for $V = 1$ mm/min or for $V = 10^4$ mm/min), the stresses suddenly decrease[7]. For all these cases, the point of sudden decrease corresponds to complete failure of the cohesive elements. From the set of results displayed in Fig. 20, we also find that, as the applied velocity becomes smaller, the macroscopic response obtained from the rate-dependent mixed-model CZM approaches the response from the rate-independent PPR CZM (Park et al. 2009).

To further investigate the effects of both the rate-dependent model parameters and loading rates, we plot the peak stress for the values of $\hat{v}$, $\hat{\lambda}_k$, and c, as a function of the applied velocity, as shown in Fig. 21. As shown by the results, the peak stress increases as the applied velocity increases, following a sigmoidal curve. One can also observe that, for lower applied velocities, the peak stresses approach the value of $\sigma_{max} = 10$ MPa, which is the cohesive strength that we used as one of the input parameters for the damage element. The results also indicate that the peak stress value for low applied velocities is independent from either $\hat{v}$, $\hat{\lambda}_k$, or c, which indicates that the slow-limit behavior is governed by the behavior of the rate-independent PPR cohesive model (Park et al. 2009). Additionally, the numerical results indicate that, as the applied velocity increases, the peak stresses approach a limit value equal to $(1+c)\sigma_{max}$. The behavior observed in either the slow-limit or fast-limit case is, by construction, consistent with the expected behavior of our model, which in the slow-limit and fast limit cases should behave as the rate-independent PPR

---

[7] We observed some convergence issues at the kink points associated with failure at the matrix/fiber interface. To circumvent these convergence issues, we used a line search technique and allowed for more Newton–Raphson iterations.
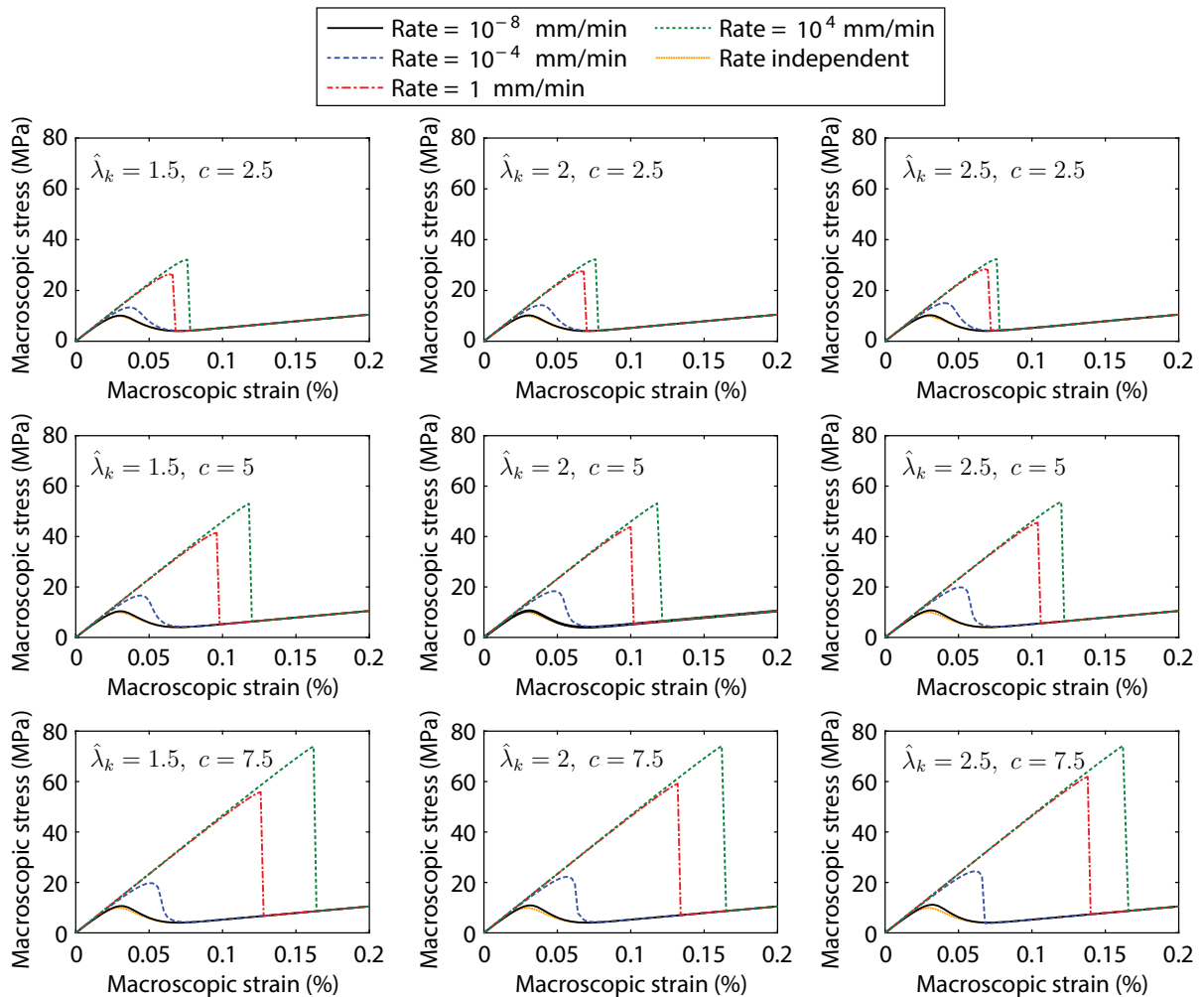
Fig. 20 Macroscopic stress–strain relationships obtained using fractional derivative of order $\hat{v} = 0.3$. The plots are presented for various springpot viscosity parameters, $\hat{\lambda}_k$, and fractional SLS model stiffness parameter, c, considering the range of applied velocity, V, from 10^{-8} to 10^4 mm/min. As the applied velocity decreases, the macroscopic response obtained from the rate-dependent CZM approaches that obtained from the rate-independent PPR CZM by Park et al. (2009) (online version in color)

model (Park et al. 2009) with initial stiffness E_k and $(1 + c)E_k$, respectively.

The order of the fractional derivative, $\hat{v}$, also affects the macroscopic behavior of the composite structure for intermediate values of the applied velocity. According to the numerical results in Fig. 21, peak stresses are more sensitive to the applied velocity when the order of the fractional derivative is smaller. In fact, we found that both peak stresses and macroscopic stress–strain curves were more sensitive to the applied velocity for lower values of $\hat{v}$. The reason for this behavior is that the relaxation modulus for the fractional SLS model

depends on the value of $\hat{v}$. As shown in Fig. 3, we observe more stress relaxation when $\hat{v}$ increases (short-term memory materials) and less stress relaxation when $\hat{v}$ decreases (long-term memory materials). The memory effect explains why macroscopic stresses are more sensitive to the applied velocity as $\hat{v}$ decreases. Based on this observation, we infer that $\hat{v}$ plays the role of a memory-like parameter, which enables us to simulate long- and short-term memory fracture processes.
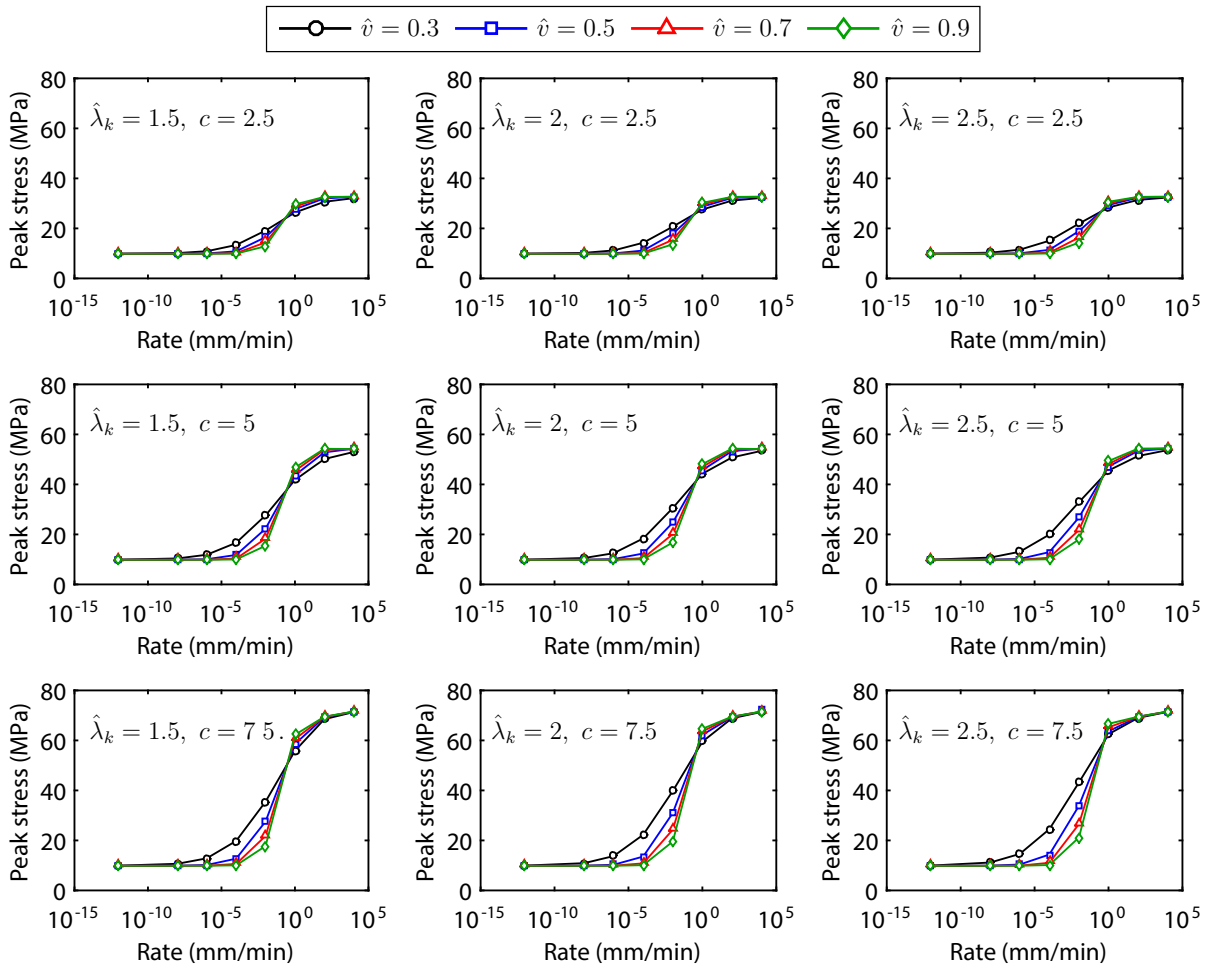
Fig. 21 Parametric space for macroscopic peak stress as a function of the applied velocity. The plots are presented for various springpot parameters, $\hat{\lambda}_k$, and fractional SLS model stiffness parameter, c, considering the range for the order of the fractional derivative from $\hat{v} = 0.3$ to $\hat{v} = 0.9$. Peak stresses behave in the form of a sigmoidal curve, and their magnitudes are highly influenced by the spring stiffness of the Maxwell arm in the fractional SLS model (online version in color)

5 Summary and conclusions

In this study, we present a mixed-mode rate-dependent cohesive zone model (CZM) that combines the features of the Park–Paulino–Roesler (PPR) cohesive model with a fractional standard linear solid (SLS) model. In our model, we obtain undamaged viscoelastic tractions from a fractional SLS model and then scale them with two damage parameters that are obtained from the PPR cohesive model (Park et al. 2009). We are able to use this model to accurately simulate rate-dependent fracture processes for a wide range of loading rates. The accuracy of the model is a direct result of the fractional SLS model, which entirely governs the rate-dependence in this CZM. In addition, we successfully approximate experimental results obtained from the rate-dependent mixed-mode fracture test by Liechti and Wu (2001), which demonstrates the capability of the model to capture rate-dependent mode-mixity dependence.

We analyze the behavior of the relaxation function of the fractional SLS model to provide physical interpretation to the order, $\hat{v}$, of the fractional differential operator. We conclude that $\hat{v}$ can be interpreted as a memory-like parameter, which allows for simulation of crack propagation problems governed by hereditary

phenomena with long- and short-term memory. This parameter strongly influences the debonding process of fiber-reinforced structures for low loading rates. When $\hat{v}$ is small (e.g., $\hat{v} < 0.3$), the macroscopic stress–strain behavior of the fiber-reinforced structures is sensitive to applied displacement rates ranging between 1×10^{-12} mm/min and 1×10^4 mm/min. However, when $\hat{v}$ is larger, our results indicate that the macroscopic stress–strain relationship is nearly insensitive to the loading rate up to approximately 1×10^{-1} mm/min. Using intermediate values for $\hat{v}$, we were able to control the rate-dependence of the CZM for intermediate loading rates. From these observations, the contribution of this work is is a model that accurately simulates rate-dependent mixed-mode fracture processes for both long- and short-term memory materials.

Appendix A Assessment of the numerical scheme used to estimate the Caputo fractional derivative

To verify the accuracy of the numerical scheme presented in Sect. 2.2 to approximate the Caputo fractional derivative of a function, $f(t)$, we rewrite Eq. (6) more compactly, as follows:

$$
{}_0D_t^{\hat{v}} f(t_N) \approx {}_0\tilde{D}_t^{\hat{v}} f(t_N) = \Delta t_N^{-\hat{v}} \sum_{j=1}^{N} (f_j - f_{j-1}) B_j,
$$

$$
B_j = \frac{\Delta t_N^{\hat{v}} (t_{N,j-1}^{1-\hat{v}} - t_{N,j}^{1-\hat{v}})}{t_{j,j-1}}, \tag{38}
$$

where $f_{j-1} = f(t_{j-1})$, $f_j = f(t_j)$, and $t_{u,v} = t_u - t_v$, $\forall\, u, v \in 0, \ldots, N$.

For the numerical assessment, we use the polynomial function $f(t) = \frac{1}{2}t^2$, for which the Caputo deriva-

tive is known in closed-form as

$$
{}_0D_t^{\hat{v}} f(t) = \frac{\Gamma(3)}{2\Gamma(3-\hat{v})} t^{2-\hat{v}}.
$$

The numerical results computed using Eq. (38) are compared with the exact Caputo derivative for various orders of the fractional derivative, $\hat{v}$. We use the unequally-spaced time grid shown in Fig. 22 to compute the fractional derivatives. As illustrated by Fig. 23, the results obtained from Eq. (38) approximate well the exact Caputo fractional derivative for all orders of the fractional derivative that we considered. To quantify the quality of the approximation, we compute the relative H^1-norm of the error between the computed and exact fractional derivatives,

$$
\epsilon^1 = \frac{\|{}_0D_t^{\hat{v}} f(t) - {}_0\tilde{D}_t^{\hat{v}} f(t)\|_1}{\|{}_0D_t^{\hat{v}} f(t)\|_1}, \tag{39}
$$

in which ${}_0\tilde{D}_t^{\hat{v}} f(t)$ refers to the approximation of ${}_0D_t^{\hat{v}} f(t)$, i.e., Eq. (38), and $\|\cdot\|_1 = \int_0^t \|\cdot\| d\tau$ is the H^1-norm of a given function. The computed errors are displayed in Table 4.

We also conduct a convergence study to determine the rate of convergence of our numerical solution. For this purpose, we use a uniform grid, such that a single time step Δt is used to obtain $t_{j+1} = t_j + \Delta t$. As conducted before, we evaluate the relative H^1-norm for $\hat{v} = 0.3$, 0.5, 0.7, and 0.9. As indicated by Fig. 24, our numerical scheme has a convergence rate of $\mathcal{O}(\Delta t^{2-\hat{v}})$.

In addition to assessing the accuracy of the proposed numerical scheme, we provide some remarks related to its computational cost. For comparison purposes, we use the numerical approximation of the *Grünwald–Letnikov* fractional derivative (Grünwald 1867), which has been used in studies by Schmidt and Gaul (2002) and Musto and Alfano (2015), to name a few. The approximation to the Grünwald–Letnikov fractional derivative is
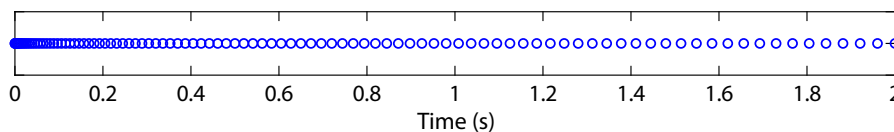

Fig. 22 Unequally spaced time discretization used to evaluate the accuracy of Eq. (38) to estimate the Caputo fractional derivative for a smooth function $f(t)$. The grid consists of 101 points (i.e., $N = 100$), such that $t_i = 2\tau_i^2$ ($i = 0, \ldots, 100$), with $\tau_{i+1} = \tau_i + 1/N$ and $\tau_0 = 0$
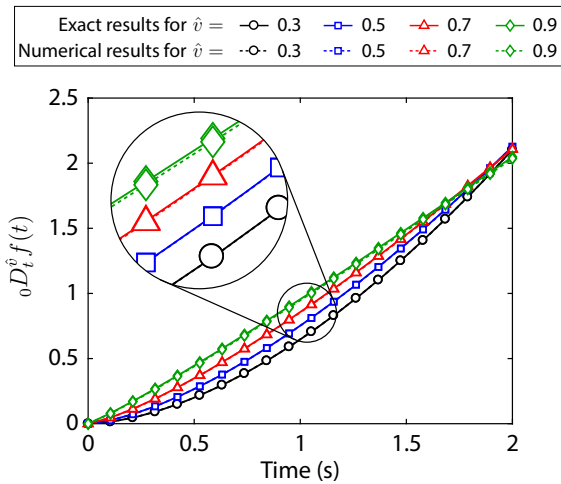
Fig. 23 Numerical and exact Caputo fractional derivative of $f(t) = \frac{1}{2}t^2$ obtained on the unequally-spaced time grid from Fig. 22. We consider various orders of the fractional derivative, $\hat{v} \in (0, 1)$

Table 4 Relative H^1-norm of the error between the computed and exact fractional derivatives for $f(t) = \frac{1}{2}t^2$ and for various orders of the fractional derivative, $\hat{v}$

$\hat{v}$	ϵ^1
0.3	3.8×10^{-4}
0.5	1.2×10^{-3}
0.7	3.2×10^{-3}
0.9	8.3×10^{-3}

$$D_t^{\hat{v}} f(t) \approx \left(\frac{t}{N}\right)^{-\hat{v}} \sum_{j=0}^{N-1} D_{j+1} f(t - jt/N),$$

$$D_{j+1} = \frac{\Gamma(j - \hat{v})}{\Gamma(-\hat{v})\Gamma(j+1)} = \frac{j - 1 - \hat{v}}{j} D_j, D_1 = 1. \tag{40}$$

To approximate a fractional derivative using either Eq. (38) or (40), we need to sum N terms, which shows that both equations scale equally as the number of grid points, N increase. However, due to the larger number of floating point operations involved in Eq. (38), its cost of evaluation is larger than that in Eq. (40). We verified this observation numerically by computing the fractional derivative of $f(t) = \frac{1}{2}t^2$ for various values of N using both Eq. (38) and (40), as depicted in Fig. 25.

Appendix B Components of the material tangent matrix for the rate-independent PPR cohesive zone model

Parameters $\hat{D}_{tt}$, $\hat{D}_{tn}$, $\hat{D}_{nt}$, and $\hat{D}_{nn}$ in Eqs. (32)–(35) are the components of the material tangent matrix for
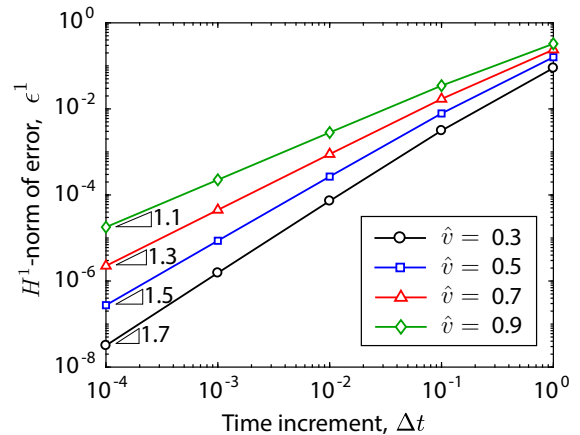

Fig. 24 Relative H^1-norm of the error between the numerical and exact Caputo derivatives of $f(t) = \frac{1}{2}t^2$, computed using Eq. (39), for various values of Δt. As observed in the results, the numerical scheme used in this study exhibits a convergence rate of $\mathcal{O}(\Delta t^{2-\hat{v}})$
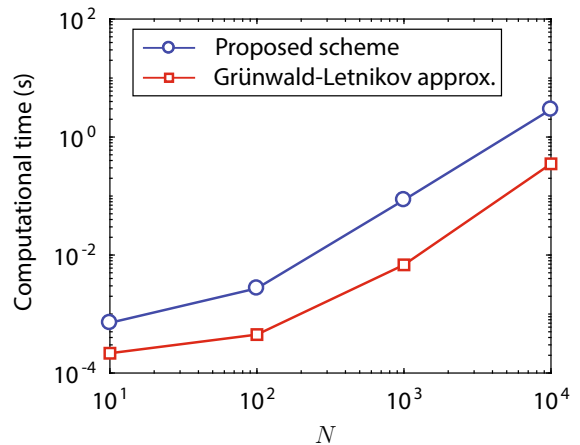

Fig. 25 Computational cost for the evaluation of a fractional derivative as a function of N. For either Eq. (38) (proposed scheme) or Eq. (40) (Grünwald–Letnikov approximation) and for each value of N, the computational time is determined as the average time required to evaluate the fractional derivative in all grid points

the rate-independent PPR cohesive zone model (Park and Paulino 2012). Because κ_n and κ_t are non-negative quantities, we write the components of the material tangent matrix for the rate independent PPR model as

$$\hat{D}_{tt}(\kappa_n, \kappa_t) = \frac{\Gamma_t}{\delta_t^2} \left[(n^2 - n) \left(1 - \frac{\kappa_t}{\delta_t}\right)^{\beta} \right.$$

$$\left(\frac{n}{\beta} + \frac{\kappa_t}{\delta_t}\right)^{n-2} + (\beta^2 - \beta) \left(1 - \frac{\kappa_t}{\delta_t}\right)^{\beta-2}$$

$$\left(\frac{n}{\beta} + \frac{\kappa_t}{\delta_t}\right)^n - 2\beta n \left(1 - \frac{\kappa_t}{\delta_t}\right)^{\beta-1} \left(\frac{n}{\beta} + \frac{\kappa_t}{\delta_t}\right)^{n-1}\right]$$

$$\left[\Gamma_n \left(1 - \frac{\kappa_n}{\delta_n}\right)^{\alpha} \left(\frac{m}{\alpha} + \frac{\kappa_n}{\delta_n}\right)^m + \langle \phi_n - \phi_t \rangle\right], \qquad (41)$$

$$\hat{D}_{tn}(\kappa_n, \kappa_t) = \hat{D}_{nt}(\kappa_n, \kappa_t)$$

$$= \frac{\Gamma_n \Gamma_t}{\delta_n \delta_t} \left[m \left(1 - \frac{\kappa_n}{\delta_n}\right)^{\alpha} \left(\frac{m}{\alpha} + \frac{\kappa_n}{\delta_n}\right)^{m-1}\right.$$

$$\left. - \alpha \left(1 - \frac{\kappa_n}{\delta_n}\right)^{\alpha-1} \left(\frac{m}{\alpha} + \frac{\kappa_n}{\delta_n}\right)^m \right]$$

$$\left[n \left(1 - \frac{\kappa_t}{\delta_t}\right)^{\beta} \left(\frac{n}{\beta} + \frac{\kappa_t}{\delta_t}\right)^{n-1}\right.$$

$$\left. - \beta \left(1 - \frac{\kappa_t}{\delta_t}\right)^{\beta-1} \left(\frac{n}{\beta} + \frac{\kappa_t}{\delta_t}\right)^n \right], \qquad (42)$$

$$\hat{D}_{nn}(\kappa_n, \kappa_t) = \frac{\Gamma_n}{\delta_n^2} \left[(m^2 - m) \left(1 - \frac{\kappa_n}{\delta_n}\right)^{\alpha} \left(\frac{m}{\alpha} + \frac{\kappa_n}{\delta_n}\right)^{m-2}\right.$$

$$\left. + (\alpha^2 - \alpha) \left(1 - \frac{\kappa_n}{\delta_n}\right)^{\alpha-2} \left(\frac{m}{\alpha} + \frac{\kappa_n}{\delta_n}\right)^m\right.$$

$$\left. - 2\alpha m \left(1 - \frac{\kappa_n}{\delta_n}\right)^{\alpha-1} \left(\frac{m}{\alpha} + \frac{\kappa_n}{\delta_n}\right)^{m-1} \right]$$

$$\left[\Gamma_t \left(1 - \frac{\kappa_t}{\delta_t}\right)^{\beta} \left(\frac{n}{\beta} + \frac{\kappa_t}{\delta_t}\right)^n + \langle \phi_t - \phi_n \rangle\right]. \qquad (43)$$

Appendix C List of symbols

α	Parameter controlling the shape of the cohesive softening curve in the normal direction
$\bar{\delta}_n$	Conjugate normal final crack opening width
$\bar{\delta}_t$	Conjugate tangential final crack opening width
β	Parameter controlling the shape of the cohesive softening curve in the tangential direction
δ_{nc}	Normal crack opening width at the peak normal traction in the original PPR model
Δ_n	Normal separation along the fracture surface
δ_n	Normal final crack opening width
Δ_n^{i+1}	Normal separation along the fracture surface at time increment $i+1$
Δ_n^i	Normal separation along the fracture surface at time increment i
δ_{tc}	Tangential crack opening width at the peak normal traction in the original PPR model
Δ_t	Tangential separation along the fracture surface
δ_t	Tangential final crack opening width
Δ_t^{i+1}	Tangential separation along the fracture surface at time increment $i+1$
Δ_t^i	Tangential separation along the fracture surface at time increment i
Γ_n	Energy constant in the PPR model
Γ_t	Energy constant in the PPR model
$\hat{\eta}_n$	Rigidity of the springpot in the normal direction
$\hat{\eta}_t$	Rigidity of the springpot in the tangential direction
$\hat{D}_{nn}, \hat{D}_{nt}$	Normal components of the material tangent stiffness matrix from the original PPR model
$\hat{D}_{tn}, \hat{D}_{tt}$	Tangential components of the material tangent stiffness matrix from the original PPR model
$\hat{T}_n$	Normal cohesive traction in the original PPR model
$\hat{T}_t$	Tangential cohesive traction in the original PPR model
$\hat{v}$	Order of the Caputo fractional derivative
κ_n	Kinematic quantity defining the maximum normal crack opening width in the history of loading
κ_n^{i+1}	Maximum normal crack opening width at time increment $i+1$
κ_n^i	Maximum normal crack opening width at time increment i
κ_t	Kinematic quantity defining the maximum absolute tangential crack opening width in the history of loading
κ_t^{i+1}	Maximum absolute tangential crack opening width at time increment $i+1$
κ_t^i	Maximum absolute tangential crack opening width at time increment i
λ_n	Parameter controlling the hardening slope of the PPR model in the normal direction
λ_t	Parameter controlling the hardening slope of the PPR model in the tangential direction
$(\dot{\ })$	Time derivative
$\langle \cdot \rangle$	Macauley bracket
$\mathbf{D}$	Material tangent stiffness matrix
ϕ_n	Fracture energy in the normal direction (with zero tangential separation)
ϕ_t	Fracture energy in the tangential direction (with zero tangential separation)
$\sigma_{\max}$	Cohesive strength in the normal direction from the original PPR model

$\tau_{\max}$	Cohesive strength in the tangential direction from the original PPR model
${}_0D_t^{\hat{v}}(\cdot)$	Caputo fractional derivative of order $\hat{v}$
${}_0I_t^{\hat{v}}(\cdot)$	Riemann–Liouville fractional integral of order $\hat{v}$
c	Stiffness parameter for the fractional SLS model
$D_{nn},\ D_{nt}$	Normal components of the material tangent stiffness matrix for the rate-dependent CZM
d_n	Normal scalar damage parameter consistent with the PPR model
$D_{tn},\ D_{tt}$	Tangential components of the material tangent stiffness matrix for the rate-dependent CZM
d_t	Tangential scalar damage parameter consistent with the PPR model
E_n	Initial stiffness parameter for the PPR model in the normal direction
E_t	Initial stiffness parameter for the PPR model in the tangential direction
m	Nondimensional exponent in the PPR model
n	Nondimensional exponent in the PPR model
S_n	Normal undamaged traction from fractional SLS model
S_t	Tangential undamaged traction from fractional SLS model
t	time
T_n	Rate-dependent cohesive traction in the normal direction
T_t	Rate-dependent cohesive traction in the tangential direction

References

ABAQUS (2011) Version 6.11 Documentation. Dassault Systemes Simulia Corp. Providence

Adolfsson K, Enelund M, Olsson P (2005) On the fractional order model of viscoelasticity. Mech Time Depend Mater 9(1):15–34

Alfano G (2006) On the influence of the shape of the interface law on the application of cohesive-zone models. Compos Sci Technol 66(6):723–730

Alfano G, Musto M (2017) Thermodynamic derivation and damage evolution for a fractional cohesive zone model. J Eng Mech 143(7):D4017001

Allen DH, Searcy CR (2001) A micromechanical model for a viscoelastic cohesive zone. Int J Fract 107:159–176

Bažant ZP, Li YN (1997) Cohesive crack with rate-dependent opening and viscoelasticity: I. Mathematical model and scaling. Int J Fract 86:247–265

Corigliano A, Mariani S, Pandolfi A (2003) Numerical modeling of rate-dependent debonding processes in composites. Compos Struct 61:39–50

Craiem D, Rojo F, Atienza J, Armentano R, Guinea G (2008) Fractional-order viscoelasticity applied to describe uniaxial stress relaxation of human arteries. Phys Med Biol 53(17):4543–4554

Dai Z, Peng Y, Mansy H, Sandler R, Royston T (2015) A model of lung parenchyma stress relaxation using fractional viscoelasticity. Med Eng Phys 37(8):752–758

Davis GB, Kohandel M, Sivaloganathan S, Tenti G (2006) The constitutive properties of the brain paraenchyma: part 2. Fractional derivative approach. Med Eng Phys 28(5):455–459

de Gennes PG (1996) Soft adhesives. Langmuir 12(19):4497–4500

Diethelm K, Ford NJ, Freed AD (2002) A predictor–corrector approach for the numerical solution of fractional differential equations. Nonlinear Dyn 29(1):3–22

Diethelm K, Ford NJ, Freed AD, Luchko Y (2005) Algorithms for the fractional calculus: a selection of numerical methods. Comput Methods Appl Mech Eng 194(6):743–773

Freed Y, Banks-Sills L (2008) A new cohesive zone model for mixed mode interface fracture in bimaterials. Eng Fract Mech 75:4583–4593

Giraldo-Londoño O, Spring DW, Paulino GH, Buttlar WG (2018) An efficient mixed-mode rate-dependent cohesive fracture model using sigmoidal functions. Eng Fract Mech 192:307–327

Gourdon E, Sauzéat C, Di Benedetto H, Bilodeau K (2015) Seven-parameter linear viscoelastic model applied to acoustical damping materials. J Vib Acoust 137(6):061003–061003–9

Grünwald AK (1867) Über "begrenzte" derivationen und deren anwendung. Zeitschrift für angewandte Mathematik und Physik 12:441–480

Johnson FA, Radon JC (1972) Molecular kinetics and the fracture of PMMA. Eng Fract Mech 4:555–576

Kang J, Bolander JE (2016) Multiscale modeling of strain-hardening cementitious composites. Mech Res Commun 78:47–54

Kapnistos M, Lang M, Vlassopoulos D, Pyckhout-Hintzen W, Richter D, Cho D, Chang T, Rubinstein M (2008) Unexpected power-law stress relaxation of entangled ring polymers. Nat Mater 7(12):997–1002

Kim H, Wagoner MP, Buttlar WG (2009) Rate-dependent fracture modeling of asphalt concrete using the discrete element method. Can J Civ Eng 36(2):320–330

Knauss WG (1970) Delayed failure—the Griffith problem for linearly viscoelastic materials. Int J Fract Mech 6(1):7–20

Knauss WG, Emri I, Lu H (2008) Springer handbook of experimental solid mechanics, Chapter 3. Springer, Berlin, pp 49–96

Kontou E, Katsourinis S (2016) Application of a fractional model for simulation of the viscoelastic functions of polymers. J Appl Polym Sci 133(23):43505

Krishnasamy VS, Mashayekhi S, Razzaghi M (2017) Numerical solutions of fractional differential equations by using fractional Taylor basis. IEEE/CAA J Autom Sin 4(1):98–106

Liechti KM, Wu J-D (2001) Mixed-mode, time-dependent rubber/metal debonding. J Mech Phys Solids 49(5):1039–1072

Mainardi F (2010) Fractional calculus and waves in linear viscoelasticity. Imperial College Press, London

Makhecha DP, Kapania RK, Johnson ER, Dillard DA, Jacob GC, Starbuck M (2009) Rate-dependent cohesive zone modeling of unstable crack growth in an epoxy adhesive. Mech Adv Mater Struct 16(1):12–19

Marzi S, Hesebeck O, Brede M, Kleiner F (2009a) A rate-dependent cohesive zone model for adhesively bonded joints loaded in mode I. J Adhes Sci Technol 23:881–898

Marzi S, Hesebeck O, Brede M, Kleiner F (2009b) A rate-dependent, elasto-plastic cohesive zone mixed-mode model for crash analysis of adhesively bonded joints. In: 7th European LS-DYNA conference, Salzburg, vol 7

Maugis D (1985) Review: subcritical crack growth, surface energy, fracture toughness, stick-slip and embrittlement. J Mater Sci 20(9):3041–3073

Maugis D, Barquins M (1978) Fracture mechanics and the adherence of viscoelastic bodies. J Phys D Appl Phys 11:1989–2023

May M, Hesebeck O, Marzi S, Böhme W, Lienhard J, Kilchert S, Brede M, Hiermaier S (2015) Rate dependent behavior of crash-optimized adhesives—experimental characterization, model development, and simulation. Eng Fract Mech 133:112–137

Miller KS, Ross B (1993) An introduction to the fractional calculus and fractional differential equations, 1st edn. Wiley, Hoboken

Milner ST, Newhall JD (2010) Stress relaxation in entangled melts of unlinked ring polymers. Phys Rev Lett 105(20):208–302

Mueller HK, Knauss WG (1971) Crack propagation in a linearly viscoelastic strip. J Appl Mech 38(2):483–488

Murio DA (2006) On the stable numerical evaluation of Caputo fractional derivatives. Comput Math Appl 51:1539–1550

Musto M, Alfano G (2013) A novel rate-dependent cohesive-zone model combining damage and visco-elasticity. Comput Struct 118:126–133

Musto M, Alfano G (2015) A fractional rate-dependent cohesive-zone model. Int J Numer Methods Eng 103(5):313–341

Needleman A (1987) A continuum model for void nucleation by inclusion debonding. J Appl Mech 54(3):525–531

Needleman A (1990a) An analysis of decohesion along an imperfect interface. Int J Fract 42(1):21–40

Needleman A (1990b) An analysis of tensile decohesion along an interface. J Mech Phys Solids 38(3):289–324

Ngo D, Park K, Paulino GH, Huang Y (2010) On the constitutive relation of materials with microstructure using a potential-based cohesive model for interface interaction. Eng Fract Mech 77:1153–1174

Ogden RW (1972) Large deformation isotropic elasticity—on the correlation of theory and experiment for incompressible rubberlike solids. Proc R Soc A 326(1567):565–584

Olard F, Di Benedetto H (2003) General "2S2P1D" model and relation between the linear viscoelastic behaviours of bituminous binders and mixes. Road Mater Pavement Des 4(2):185–224

Oldham KB, Spanier J (1974) The fractional calculus: theory and aapplication of differentiation and integration to arbitrary order, vol 111. Mathematics in science and engineering. Academic Press, Cambridge

Padovan J (1987) Computational algorithms for FE formulations involving fractional operators. Comput Mech 2(4):271–287

Park K, Paulino GH (2011) Cohesive zone models: a critical review of traction–separation relationships across fracture surfaces. Appl Mech Rev 64(6):061002

Park K, Paulino GH (2012) Computational implementation of the PPR potential-based cohesive model in Abaqus: educational perspective. Eng Fract Mech 93:239–262

Park K, Paulino GH, Roesler JR (2009) A unified potential-based cohesive model for mixed-mode fracture. J Mech Phys Solids 57:891–908

Podlubny I (1998) Fractional differential equations: an introduction to fractional derivatives, fractional differential equations, to methods of their solution and some of their applications. Academic press, Cambridge

Rahul-Kumar P, Jagota A, Bennison SJ, Saigal S, Muralidhar S (1999) Polymer interfacial fracture simulations using cohesive elements. Acta Materialia 47(15–16):4161–4169

Reeder JR, Crews JR (1990) Mixed-mode bending method for delamination testing. AIAA J 28:1270–1276

Rubinstein M, Obukhov SP (1993) Power-law-like stress relaxation of block copolymers: disentanglement regimes. Macromolecules 26(7):1740–1750

Schiessel H, Blumen A (1993) Hierarchical analogues to fractional relaxation equations. J Phys A Math Gen 26(19):5057–5069

Schiessel H, Blumen A (1995) Mesoscopic pictures of the sol–gel transition: ladder models and fractal networks. Macromolecules 28(11):4013–4019

Schiessel H, Blumen A, Alemany P (1994) Dynamics in disordered systems. Progr Colloid Polym Sci 96:16–21

Schiessel H, Metzler R, Blumen A, Nonnenmacher TF (1995) Generalized viscoelastic models: their fractional equations with solutions. J Phys A Math Gen 28(23):6567–6584

Schmidt A, Gaul L (2002) Finite element formulation of viscoelastic constitutive equations using fractional time derivatives. Nonlinear Dyn 29(1):37–55

Scott-Blair GW (1947) The role of psychophysics in rheology. J Colloid Sci 2(1):21–32

Shen B, Paulino GH (2011a) Direct extraction of cohesive fracture properties from digital image correlation: a hybrid inverse technique. Exp Mech 51:143–163

Shen B, Paulino GH (2011b) Identification of cohesive zone model and elastic parameters of fiber-reinforced cementitious composites using digital image correlation and a hybrid inverse technique. Cem Concr Compos 33:572–585

Spring DW, Giraldo-Londoño O, Paulino GH (2016) A study on the thermodynamic consistency of the Park–Paulino–Roesler (PPR) cohesive fracture model. Mech Res Commun 78:100–109

Tosun-Felekoğlu K, Felekoğlu B, Ranade R, Lee BY, Li V (2014) The role of flaw size and fiber distribution on tensile ductility of PVA-ECC. Compos Part B Eng 56:536–545

Uchaikin VV (2013) Fractional derivatives for physicists and engineers, vol 1. Springer, Berlin

Valoroso N, Debruyne G, Laverne J (2014) A cohesive zone model with rate-sensitivity for fast crack propagation. Mech Res Commun 58:82–87

Volokh KY (2004) Comparison between cohesive zone models. Commun Numer Methods Eng 20(11):845–856

Webb TW, Aifantis EC (1995) Oscillatory fracture in polymeric materials. Int J Solids Struct 32(17–18):2725–2743

Welch S, Rorrer R, Duren R (1999) Application of time-based fractional calculus methods to viscoelastic creep and stress relaxation of materials. Mech Time Depend Mater 3(3):279–303

Williams JG (1972) Visco-elastic and thermal effect on crack growth in PMAA. Int J Fract Mech 8(4):393–401

Williams ML (1963) The fracture of viscoelastic material. In: Drucker DC, Gilman JJ (eds) Fracture of solids. Interscience Publishers, New York, London, pp 157–188

Williams ML (1965) Initiation and growth of viscoelastic fracture. Int J Fract Mech 1:292–310

Wu J-D (1999) Time-dependent, mixed-mode fracture of solid rocket motor bondline systems. Ph. D. thesis, University of Texas at Austin

Xu XP, Needleman A (1993) Void nucleation by inclusion debonding in a crystal matrix. Model Simul Mater Sci Eng 1(2):111–132

Xu C, Siegmund T, Ramani K (2003a) Rate-dependent crack growth in adhesives I. Modeling approach. Int J Adhes Adhes 23:9–13

Xu C, Siegmund T, Ramani K (2003b) Rate-dependent crack growth in adhesives II. Experiments and analysis. Int J Adhes Adhes 23:15–22

Zhou F, Molinari JF, Shioya T (2005) A rate-dependent cohesive model for simulating dynamic crack propagation in brittle materials. Eng Fract Mech 72:1383–1410

Zhu Y, Liechti KM, Ravi-Chandar K (2009) Direct extraction of rate-dependent traction–separation laws for polyurea/steel interfaces. Int J Solids Struct 46(1):31–51